Angle Resolved Polarization and Vibrational Studies of Transition Metal Trichalcogenides and Related Alloys

by

Wilson Kong

A Thesis Presented in Partial Fulfillment
of the Requirements for the Degree
Master of Science

Approved April 2017 by the
Graduate Supervisory Committee:

Sefaattin Tongay, Chair
Liping Wang
Matthew Green

ARIZONA STATE UNIVERSITY

May 2017

ABSTRACT

A new class of layered materials called the transition metal trichalcogenides (TMTCs) exhibit strong anisotropic properties due to their quasi-1D nature. These 2D materials are composed of chain-like structures which are weakly bound to form planar sheets with highly directional properties. The vibrational properties of three materials from the TMTC family, specifically TiS_3, ZrS_3, and HfS_3, are relatively unknown and studies performed in this work elucidates the origin of their Raman characteristics. The crystals were synthesized through chemical vapor transport prior to mechanical exfoliation onto Si/SiO_2 substrates. XRD, AFM, and Raman spectroscopy were used to determine the crystallinity, thickness, and chemical signature of the exfoliated crystals. Vibrational modes and anisotropic polarization are investigated through density functional theory calculations and angle-resolved Raman spectroscopy. Particular Raman modes are explored in order to correlate select peaks to the b-axis crystalline direction. Mode III vibrations for TiS_3, ZrS_3, and HfS_3 are shared between each material and serves as a unique identifier of the crystalline orientation in MX_3 materials. Similar angle-resolved Raman studies were conducted on the novel $Nb_{0.5}Ti_{0.5}S_3$ alloy material grown through chemical vapor transport. Results show that the anisotropy direction is more difficult to determine due to the randomization of quasi-1D chains caused by defects that are common in 2D alloys. This work provides a fundamental understanding of the vibrational properties of various TMTC materials which is needed to realize applications in direction dependent polarization and linear dichroism.

I dedicate this work to my mother, father, sister, grandmother, and my entire extended family. Without their love and support, I would not have risen to become the first STEM graduate in our family.

ACKNOWLEDGMENTS

I wish to express my sincere appreciation to my advisor, Dr. Sefaattin Tongay, for accepting me into his group, providing support in both my academics and personal life, and shaping me into a more capable researcher. His vast knowledge of 2D materials and accommodating attitude has eased the difficulty of my research projects. I cannot think of a better advisor to supervise and mentor me during my time at Arizona State University.

I would like to thank each of my many lab group members, both past and present, for all of your guidance and assistance on my various research projects. Your work ethic and knowledge served as a strong model for me to follow as a young graduate student. Not only was the work in this group productive, it was very enjoyable. You were a fantastic group of people to spend the last two years with.

I would also like to thank the various collaborators from ASU and other universities for your contributions to my research and for providing me with excellent results. Special thanks to Dr. Hasan Sahin, Mr. David Wright, and Mr. Cihan Bacaksiz for your tremendous contributions towards making my first journal publication possible.

Lastly, I want to thank my family for all the love and support they have shown me throughout my entire life. I am the person I am today because of you.

TABLE OF CONTENTS

Page

LIST OF FIGURES

Figure Page

CHAPTER 1

1. INTRODUCTION

1.1 Two-Dimensional Materials

In recent years, the field of nanomaterials has gained much attention due to the study of an emerging class of layered materials known as two-dimensional (2D) materials [1]. Layered materials are comprised of atomically thin sheets with a thickness of one unit cell bound together through weak Van der Waals interactions [2]. This enables the facile separation of individual atomic sheets from a bulk crystal either through mechanical or liquid exfoliation techniques [3–6]. Pristine surfaces of 2D materials are minimally rough, contain few dangling bonds, and generally free of defect sites [7]. Such chemically passivated surfaces enables the formation of vertical heterostructures between several types of layered materials [8]. Advances in bottom-up synthesis methods such as chemical vapor deposition (CVD) [9], physical vapor deposition (PVD) [10], and molecular beam epitaxy (MBE) [11] improve the scalability of these materials for additional research purposes or to one day achieve commercial production.

Unique mechanical, electronic, and optical properties derived from strong quantum confinement effects are seen in 2D materials [12]. Much of this research began when physicists Andre Geim and Konstantin Novoselov first discovered the widely known and popular 2D material, graphene [13]. This material and its superior properties enable its many applications in optoelectronics [14], electrochemical energy storage [15], and

coatings for aircraft [16]. Despite the merits of graphene, this 2D material still faces many limitations that prevent it from achieving greater potential applications. Many other discovered 2D materials beyond graphene possess electronic properties that range from insulating and semiconducting to metallic or even superconducting [17]. Hexagonal boron nitride (h-BN) is an analogue to graphene, possessing a hexagonal crystal structure and a wide band gap ranging from 3.6 to 7.1 eV [18]. Graphene is known to be synthesized on h-BN sheets due to their similar lattice constants and surface structure [19,20]. Environmentally unstable 2D materials use h-BN as a passivation layer to protect it from oxidation or other destructive processes.

Other commonly studied 2D materials include the semiconducting transition metal dichalcogenides (TMDCs) with layer dependent optical and electronic behavior [21]. Lamellar TMDCs span a wide range of band gap values which make them attractive candidates for device fabrication. Vertical and lateral heterojunction growth of layered materials leads nano-scale field-effect transistors with strong interlayer excitonic transitions and enhanced photoluminescence (PL) [22,23]. Even beyond TMDCs, elemental layered materials, (phosphorene, silicene, etc.) [24], transition metal monochalcogenides (GaSe, InSe, etc.) [25-29], anisotropic materials (ReS_2, $ReSe_2$, etc.) [30–34], and 2D covalent organic frameworks [35] add to the increasingly large number of 2D materials available. Such a wide variety of low dimensional materials, potential applications, and novel synthesis methods encourage the development of many new fields of materials research. In the following sections, many notable 2D materials are discussed in greater detail to illuminate their importance to materials science research.

1.1.1 Graphene

Graphene is a single sheet of carbon atoms with a sp^2 hybridization arranged in a hexagonal crystal lattice. Upon its introduction as a single atomic layer from graphite through mechanical exfoliation techniques, the study of graphene became the progenitor of 2D materials research. Physicists Andre Geim and Konstantin Novoselov successfully isolated a monolayer of graphene which earned them the 2010 Nobel Prize in Physics. Many materials properties of graphene are not observed in bulk graphite such as a high electronic mobility of 100,000 $cm^2\ V^{-1}\ s^{-2}$ [13], a tensile modulus of 1 TPa [36], which is the highest of any known material, impermeability [37], and high optical transparency [38]. Chemically inert and mechanically flexible, graphene's unique properties are necessary for the improvement or development of advanced super capacitors [39], water filtration devices [40], or flexible electronics [12].

Graphene is additionally known as a zero-gap semiconductor material. The electronic band structure of graphene at the high symmetry points of the Brillouin zone form a Dirac cone where valence and conduction bands display a linear dispersion and meet at a single point [41]. This linear dispersion enables graphene to possess such a high electronic mobility with carriers behaving as massless Dirac fermions [42]. However, graphene's lack of a band gap limits its use in field effect transistors, optoelectronics, or any applications requiring switching capabilities. Inducing a band gap into graphene requires the use of strain engineering or the formation of graphene into nano-ribbons [20,43,44]. Nonetheless, graphene serves as a strong starting point to begin understanding the behavior of low dimensional materials.

1.1.2 Transition Metal Dichalcogenides

Analogous to graphene, transition metal dichalcogenides (TMDCs) are layered materials that potentially serve as attractive alternatives for device applications. TMDCs circumvent graphene's limitations by offering a similar flexible structure and a tunable range of band gap energies [45]. A typical TMDC material is characterized by the chemical formula, MX_2 where M is a transition metal (i.e. Mo, W), and X is an element from the chalcogen family (i.e. S, Se, Te). Metal atoms are arranged in a trigonal or octahedral prismatic coordination. Overall, TMDC crystals generally have hexagonal or rhombohedral crystal structures with behaviors that range from semiconducting to metallic.

First principles calculations show the TMDC band structure for MoX_2 and WX_2 undergoing an indirect to direct band transition as the thickness decreases from bulk to a monolayer. The change in electron hybridization due to quantum confinement effectively changes the band structure of these materials as the number of layers change. For WS_2, the band gap energy ranges from 1.1 to 1.9 eV as the bulk crystal is thinned down to a monolayer [12]. These electronic and optical properties can be further tuned through strain engineering [46], defect engineering [47], doping [7], or alloying [48].

Few-layer TMDCs have been explored in the fabrication of FETs [8,22,23,49], as a potential replacement for platinum as a catalytic material [50,51], in atomically thin photovoltaics [52], and in label-free biosensors [53]. Due to the unique band structure of TMDCs, the confinement of carriers at the conduction and valance band extrema leads to potential applications in valleytronics [54]. One of the primary challenges to utilizing these properties is being able to synthesize TMDCs in large quantities. While exfoliation

produces limited area, yet pristine single crystals of few-layer sheets, the advancement of vapor deposition techniques will ultimately dictate the scalability of these materials.

1.1.3 Transition Metal Monochalcogenides

Materials similar to TMDCs, transition metal monochalcogenides (TMMCs) are layered materials that are known to exhibit nonlinear optical behavior. TMMCs follow the standard chemical formula MX (M = Ga, In, Sn and X = S, Se, Te). The layered structures are composed of atoms bonded in the following X-M-M-X orientation either with hexagonal or rhombohedral crystal structure. In contrast to TMDCs, TMMCs are direct gap semiconductors in bulk form that transition to an indirect gap for flakes fewer than 7 layers [55].

Gallium selenide (GaSe) is a layered semiconductor with a direct band gap energy of 2 eV [28,56]. Large band renormalization for GaSe can be seen on monolayers grown onto silicon (111) through Van der Waals epitaxy. Precise control over kinetic factors such as cooling rates can alter the growth morphologies of few-layer GaSe [57]. Most notably, the second harmonic generation (SHG), a nonlinear optical process, seen in GaSe is strongest of all known 2D materials, being 1 to 2 orders of magnitude larger than MoS_2 monolayers [25].

Indium selenide (InSe) is another layered semiconductor exhibiting a direct to indirect gap transition as the thickness of the material decreases. Recent reports have shown few layer InSe possessing light electron mass and high mobility values of up to 2000 $cm^2 V^{-1} s^{-1}$ at low temperature values [58]. InSe is additionally explored for its thickness

dependent nonlinear optical phenomena. As a monolayer, InSe is known to be unstable in an oxygen rich atmosphere. Encapsulation of InSe with graphene or h-BN is necessary for InSe optical properties to be explored or photodetectors to be fabricated [59].

1.2 Anisotropic Two-Dimensional Materials

Another class of 2D materials offer additional advantages to traditional layered materials which primarily consist of structurally isotropic sheets. These materials possess structural anisotropy which enable their materials properties to become highly dependent on their crystalline orientation. Examples of anisotropic 2D materials include phosphorene, the monolayer form of black phosphorus (BP), rhenium disulfide (ReS_2), gallium telluride (GaTe), and the transition metal trichalcogenides (TMTCs). Physical properties such as electronic mobility or mechanical strength generally hold larger values along the anisotropic direction.

1.2.1 Black Phosphorus and Phosphorene

Black phosphorus (BP) is an allotrope of the element phosphorus which is thermodynamically stable at room temperature. BP crystallizes in an orthorhombic structure and is analogous to graphite in its color, layered structure, and electrical conductivity [60]. Each phosphorus atom is connected to three other adjacent atoms to form linked rings with reduced in-plane symmetry. Structural anisotropy in each layer of BP leads to direction dependent properties. Phosphorene, the monolayer form of BP, is known

to exhibit linearly polarized two-lobed plots for PL which indicate a direction dependent polarization response to light [61]. Thickness dependent band gap energies spanning from 0.3 eV for bulk BP and 2.0 eV for phosphorene effectively connects the band gap range between graphene and the TMDCs [62]. Anisotropic carrier mobility values can be seen for few layered BP measured from 10K to 300K [63]. The x-direction shows light effective-mass values which make this an attractive materials for high performance transistors. However, monolayer phosphorene is not environmentally stable with hinders its use in many device applications unless encapsulated by an inert barrier material.

1.2.2 Rhenium Disulfide and Gallium Telleride

Rhenium disulfide (ReS_2) is another member of the TMDC family which distinguishes itself from other TMDCs like MoS_2 through its anisotropic crystal structure and direction dependent properties. These layered materials stack via Van der Waals forces with strong covalent bonding within each planar sheet. Structural in-plane anisotropy originates from the strong dimerization and interaction of adjacent Re atoms. This feature enables ReS_2 to be used in linear dichroic applications. ReS_2 is known to have optical band gaps ranging from 1.4 to 1.6 eV as the material is thinned from bulk to monolayer [34]. Recently, it has been shown that CVD grown truncated triangular and hexagonal ReS_2 flakes contain oriented sub-domains with Re-Re chains arranged in particular directions with respect to the nucleation center [64]. High resolution scanning transmission electron microscopy (HRSTEM) studies provide strong insight into the atomic restructuring of

chains at grain boundaries due to vacancy defects. Re-chains are known to change direction near grain boundaries which can reduce the anisotropic polarization response of ReS_2 nanosheets.

Monoclinic gallium telluride (GaTe) is another layered material belonging to the transition metal monochalcogenide family. Unlike GaSe, a structurally isotropic material, GaTe sheets have reduced in-plane symmetry. Each primitive unit cell contains 6 Ga and 6 Te atoms with a C2/m symmetry. This material has a direct band gap of 1.65 eV with additional emission lines shown at 1.29, 1.39, and 1.5 eV [65]. Its strong in-plane anisotropic polarization has been demonstrated through angle-resolved photoluminescence (ARPL) [66]. The incident laser light polarized along the GaTe flake achieves its maximum when the polarization direction is parallel to <010> chain direction which indicates maximum optical absorbance along this direction. GaTe also exhibits bright PL emission in the forbidden energy band which has not been previously reported [65]. Researchers have recently synthesized this material through a physical vapor transport (PVT) method on various substrates which demonstrates the versatility of vapor phase grown anisotropic materials [65].

1.2.3 Transition Metal Trichalcogenides

Transition metal trichalcogenides (TMTCs) are a new class of layered materials with the chemical formula MX_3 where M is a transition metal from group IVB (i.e. Ti, Zr, Hf) or group VB (i.e. Nb, Ta) and X is an element from the chalcogen family (i.e. S, Se,

Te). These materials primarily crystalize in a monoclinic crystal structure with a few exceptions in NbS_3 (triclinic) and TaS_3 (orthorhombic or monoclinic) [67]. Several crystal variants exist for TMTCs including the $ZrSe_3$ type (A variant) or TiS_3 type (B variant) [68]. The monoclinic structures have a $p2_{1/m}$ space group symmetry with unit cells containing 2 metal atoms and 6 chalcogen atoms. Each metal atom is covalently bonded to 6 other chalcogen atoms in a trigonal prismatic configuration. In-plane dimerization of sulfur atoms leads to these MX_6 cells to form chains along the b-axis direction. Each trigonal prismatic chain is shifted by half a lattice parameter length along the chain axis.

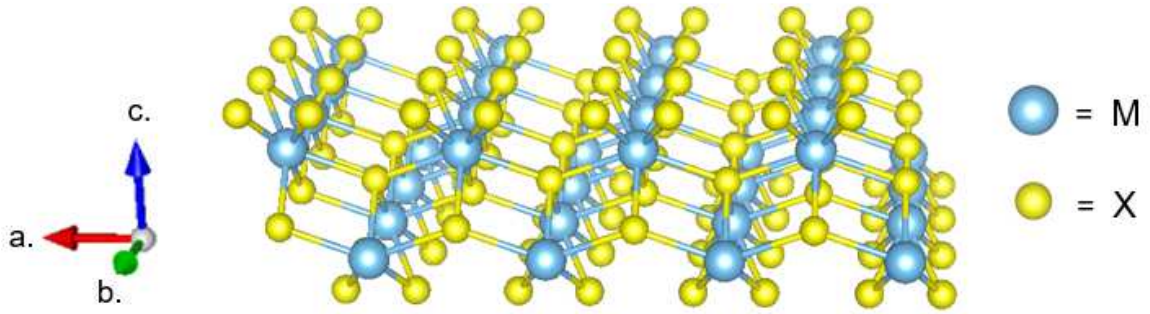

Figure 1. 3D representation of a typical MX_3 crystal structure.

Like many other layered 2D materials, each individual layer stacks via Van der Waals forces which allows for the isolation of ultra-thin flakes. However, unlike conventional isotropic materials, TMTC sheets are the result of the cation and anion bonding of adjacent chains along the a-axis direction. Covalent bonding of metal and chalcogen atoms in the b-axis direction is much stronger than bonding in the a-axis direction which is the primary cause of weak inter-chain interactions. This weak chain interaction allows TMTC crystals to cleave in rectangular nano-ribbon shapes, often with

a visibly long edge parallel to the b-axis direction of the flake. Typically, TMTC crystals grow along this b-axis direction which leads to whisker or hair-like growth.

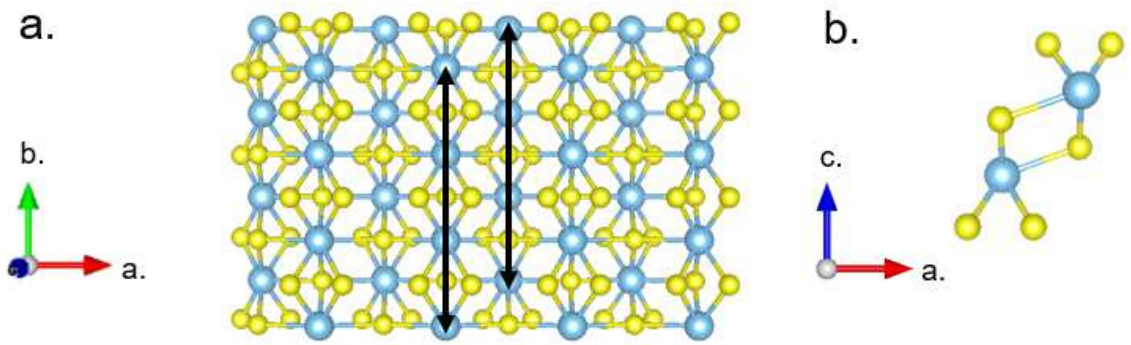

Figure 2. a) Top down view of MX_3 chain direction along the b-axis shown with black arrows. b) Bonding between adjacent chains in the a-c plane.

The chain-like structures impart a quasi-1D behavior, similar to nanowires or nanotubes, to TMTC materials which subsequently show anisotropic properties for a 2D material. TiS_3 mobility is known to be strongest along the b-axis at 80 $cm^2 V^{-1} s^{-1}$ while showing a weaker response along the a-axis at 40 $cm^2 V^{-1} s^{-1}$ [69]. ZrS_3 is known to show strong linear dichroism along its b-axis direction when laser polarization is parallel to the chains [70]. Under strained conditions, HfS_3 transitions from an indirect to direct band gap semiconductor [71]. Much of this quasi-1D behavior affords TMTCs a variety of applications in FETs, photodetectors, and other photonic devices.

TMTCs represent a system of 2D materials with greater advantages over traditional 2D materials. However, a fundamental understanding of their vibrational properties is still being pioneered. Knowledge of TMTC characteristic vibrations would provide greater insight into their unique materials properties. The following questions are addressed in this

work which provide a greater understanding of TMTCs: What is the origin of the Raman peaks for TMTCs? Do TMTCs have similar vibrational characteristics? Can these vibrational characteristics be used to correlate particular Raman peaks to the b-axis chain direction? Is the anisotropy response thickness dependent? Does the anisotropy of TMTCs change when alloyed? This study employs density functional theory (DFT) calculations and angle-resolved Raman spectroscopy in order to shed light onto the vibrational characteristics and polarization of TMTCs which will establish a foundation of knowledge for researchers to build upon.

CHAPTER 2

2. CRYSTAL GROWTH AND CHARACTERIZATION

2.1 Chemical Vapor Transport

2.1.1 Methodology

Bulk crystals of layered materials have been synthesized through a variety of techniques. The commonly used Bridgman-Stockbarger growth method employs a vertical furnace with a temperature gradient. Semiconductors such as GaAs can be grown through this technique where the Czochralski process proves to be more challenging. Chemical vapor transport (CVT) is a common method used to synthesize bulk semiconductor crystals in research or industrial settings. Many of the transition metal chalcogenides are grown using this technique [72,73]. The crystal growth utilizes elemental precursors or chemical compounds that are sealed in one end of an evacuated quartz ampoule. The reactions take place in a heated tube furnace where the contents in the quartz ampoule are evaporated and transported with or without the use of a chemical transport agent such as iodine gas. This growth method makes use of a temperature gradient where reactions are classified based on the thermodynamics between the solid material and the transporting agent. Exothermic reactions occur when the solid material is transported from a cooler temperature to a higher temperature where growth is favorable. Endothermic reactions takes place with materials transported from high to low temperature zones. Crystal growth typically takes place over

a period of several days. Safety is of prime concern during this crystal growth process so growth temperatures are typically achieved at a slow heating rate to prevent any explosive events from occurring.

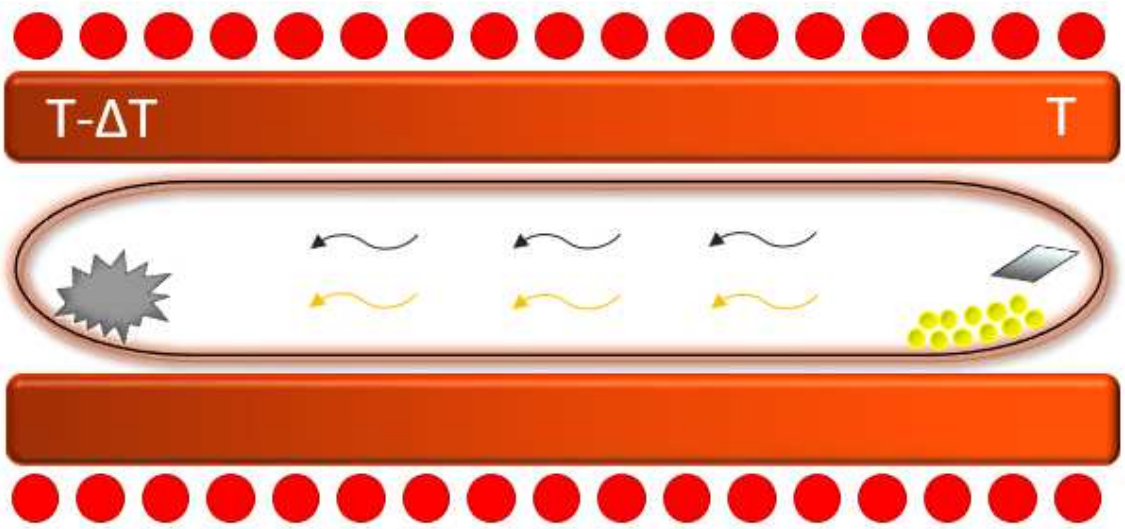

Figure 3. Schematic of typical CVT growth of TMTC crystals within a horizontal tube furnace.

2.1.2 Growth of MX_3 Materials

Utilizing the chemical vapor transport method, the following TMTC materials have been synthesized in a bulk crystal form: TiS_3, ZrS_3, and HfS_3. Despite being similar materials, each TMTC was grown with different experimental conditions such as growth temperature and growth time. For each crystal growth, a quartz ampoule measuring 210 mm in length and 15 mm in diameter was used to contain the precursor materials. A stoichiometric ratio for the precursors was kept at 1:3. Prior to growth, the quartz ampoules containing precursors in one end were evacuated to a vacuum level of 10^{-6} Torr. It is

advised to inspect the quartz ampoules for surface flaws and to remove any contaminants such as oxygen during the evacuation and sealing process. This prevents the possibility of damage to the ampoule or production of low quality crystals. Sealed ampoules were placed into a two-zone horizontal tube furnace where the precursor materials are kept at the high temperature zone. Crystal growth occurs along the inner walls of the quartz ampoule as the evaporated precursors react at the cooler temperature zone. A temperature gradient of 100 °C was maintained between the hot zone and the growth temperature for a distance of 20 cm. A slow heating rate of 2 °C per minute was used to prevent highly destructive reactions from taking place. To remove the crystals from the ampoule, a band saw was used to unseal the tube. The growth conditions specific to each crystal are outlined in the following sections.

2.1.3 Titanium Trisulfide Growth

TiS_3 bulk crystals were synthesized using titanium sheets with excess sulfur pellets placed into a quartz ampoule evacuated to 10^{-6} Torr. The precursor amount totaled 1 g with the constituents kept at a metal-sulfur molar ratio of 1:3. The crystal growth was conducted in a two-zone horizontal tube furnace which was heated to a temperature of 520 °C and maintained at this temperature for a period of 5 days. The quartz ampoule cooled naturally to room temperature after the 5 day period. Upon inspection, the grey TiS_3 crystals appear needle-like which is expected from their anisotropic crystal structure (figure 4).

Figure 4. TiS_3 crystals grown on the inner walls of a quartz ampoule.

2.1.4 Zirconium and Hafnium Trisulfide Growth

ZrS_3 and HfS_3 bulk crystals are synthesized using the same growth conditions. As with TiS_3, each quartz ampoule was loaded with zirconium and hafnium sheets with excess sulfur pellets that totaled 1 g. The stoichiometric ratio was kept at 1:3. After evacuating the ampoules to 10^{-6} Torr, they were placed into a two-zone horizontal tube furnace which was heated to a temperature of 650 °C. The crystals were grown in a 5 day period and cooled down naturally to room temperature. ZrS_3 crystals are also needle-like and similar in appearance to TiS_3 crystals. HfS_3 crystals, however, appeared gold with the same needle-like structure (figure 5).

Figure 5. HfS_3 crystals grown on the inner walls of a quartz ampoule.

2.2 Sample Preparation

Silicon pieces with a thermally grown oxide layer 295 nm thick are prepared as substrates for the TMTC crystals to be exfoliated onto for materials characterization. The silicon (111) wafers were cleaved using a diamond-tip pen into 0.5 by 0.5 cm square shards. The substrates were placed into an oxygen plasma etcher for 3 minutes in order to remove any surface contamination prior to the exfoliation process.

Mechanical exfoliation has been one of the primary methods used to isolate individual layers of a layered crystal. The success of Dr. Geim and his team in isolating monolayer graphene promoted the use of this technique on other layered materials. For sample preparation, several pieces of Scotch tape was used to successively peel apart the layered crystals until a somewhat translucent film of crystals remained on the tape. The tape was adhered to the prepared silicon substrates with a small amount of pressure and the

Van der Waals interaction with the SiO_2 surface transfers MX_3 flakes to the substrate. Using an optical microscope, flakes were identified as ribbon-like pieces (figure 6). The color contrasts of the crystals on the SiO_2/Si substrates acts as a guide for the relative thickness of the flakes. Generally brighter colors (yellow or red) indicate thick flakes whereas darker colors (dark blue or violet) indicate thin flakes [74].

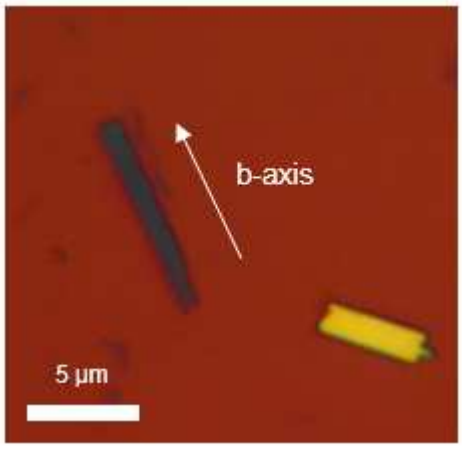

Figure 6. Optical image of a ZrS_3 flake with the b-axis direction shown.

2.3 Materials Characterization

Upon transfer to Si/SiO_2 substrates, various characterization techniques were used to identify their crystallinity, thickness, and chemical signature. To this end, X-ray powder diffraction (XRD), atomic force microscopy (AFM), and Raman spectroscopy were utilized. A brief overview of each technique is introduced prior to discussion of the experimentally obtained data.

2.3.1 X-Ray Powder Diffraction

X-ray powder diffraction (XRD) is an analytical technique used to obtain information about the atomic or molecular structure of a material. An incident x-ray beam of wavelength λ is diffracted into various directions depending on the orientation of atoms and interplanar spacing (d_{hkl}) in a crystal. The main principle behind XRD is the theory of Bragg diffraction where the x-ray wavelength is directly proportional to d_{hkl} and the sine of the angles (θ_{hkl}) that produce a constructive interference. These relations are summarized in the following equation (Bragg's Law):

$$n\lambda = 2d_{hkl}sin\theta_{hkl} \tag{2.1}$$

TMTC crystals were examined under a Siemens D5000 x-ray diffractometer using Cu Kα irradiation wavelength of λ = 1.54 Å. For measurements, a small piece of sample crystal was mounted onto a zero-background plate and the 2θ angle ranging from 5 to 65 degrees. The collected XRD spectrum for TiS_3, ZrS_3, and HfS_3 is shown in this figure. The ICDD card data for each material matches with the obtained peaks confirming their monoclinic structure. The sharp peaks for each material indicate a highly crystalline structure. Lattice parameters for TiS_3 are as follows: a = 4.97 Å, b = 8.71 Å, c = 3.43 Å. Lattice parameters for ZrS_3 are as follows: a = 5.12 Å, b = 8.98 Å, c = 3.62 Å. Lattice parameters for HfS_3 are as follows: a = 5.09 Å, b = 8.97 Å, c = 3.59 Å.

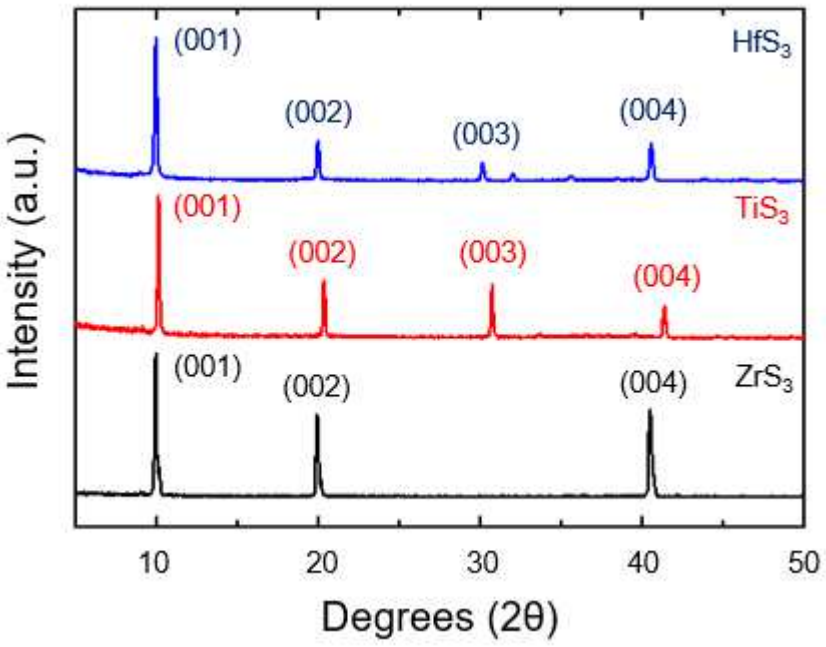

Figure 7. Plot of XRD peaks for TiS_3, ZrS_3, and HfS_3.

2.3.2 Atomic Force Microscopy

Atomic force microscopy (AFM) is a variation of scanning probe microscopy which is able to achieve resolutions on the order of nanometers. Primarily, AFM is used for imaging of materials, force measurements, and surface manipulation of a material. An AFM probe consists of a silicon or silicon nitride cantilever with a chemically etched tip. A laser is reflected off of the back end of the cantilever as it translates across the surface of the material in contact mode, non-contact mode, or tapping mode. The laser position is collected through a photodetector and a computer processes the signals into an image of the surface or material.

Atomic force microscopy for the TMTC flakes was conducted using the Dimension Multimode 8 under tapping mode. The resolution was set at 256 × 256, and the

scanning rate was typically set to at 1.0 Hz; which could change depending on the overall lateral area of the flake measured. This technique allowed for the accurate identification of thin flakes (less than 10 nm) for angle-resolved Raman studies which will be discussed later. Below is a typical AFM image of a TMTC flake, specifically for TiS_3, which is observed to be ~5 nm thick.

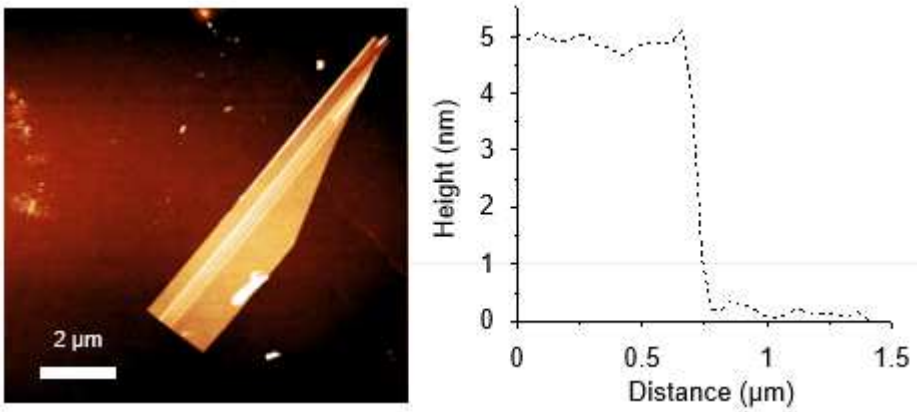

Figure 8. AFM image of TiS_3 flake with a height profile.

2.3.3 Raman Spectroscopy

Raman spectroscopy is a non-destructive optical technique that has become an important method for probing the elementary excitations (phonons or plasmons) in a solid material. It is a common fingerprinting tool for chemical compounds which provides both qualitative and quantitative information. Raman bands come from the oscillation of induced dipoles due to an interaction with light. The resulting spectra is graphically represented in the form of peaks at certain frequency values (measured in cm^{-1}). This

characterization technique is particularly useful in 2D materials systems since information can be obtained for crystallinity, thickness, domain size, or defects present [75].

Inelastic scattering of light due to elementary excitations is the basis behind this optical technique. When photons from a monochromatic light source is incident upon a material, one of two inelastic scattering processes occurs. For Stokes scattering, photons lose some of their energy to lattice vibrations (phonons) in the material; in contrast, photons during anti-Stokes scattering gain energy from surrounding phonons. The scattered light is collected through a charge coupled detector (CCD) and the signal is processed on a computer to generate a plot showing peak intensity vs wavenumber. The intensity of the peaks and their full width at half maximum (FWHM) illustrate the relative quantity and crystallinity of the material respectively. Measurements can be made on isolated spots on the material or across a selected area during Raman mapping.

A Renishaw InVia Raman spectrometer equipped with a 15mW, 488 nm laser and a 100x objective lens was used. Measurements on TiS_3, ZrS_3, and HfS_3 flakes using the 488 nm laser generate four characteristic peaks for each material as seen in the figure below. The peak shown at a wavenumber of 521 cm^{-1} is a characteristic peak of the silicon substrate. TMTC Raman spectra matches experimentally obtained results from literature and will be discussed in greater detail in the next chapter.

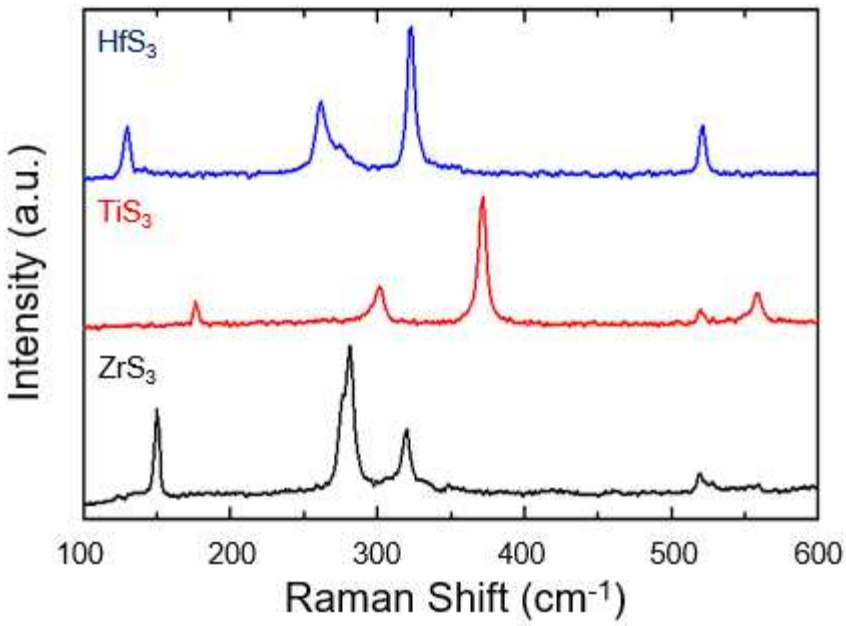

Figure 9. Raman spectra of HfS_3, TiS_3, and ZrS_3 crystals.

CHAPTER 3

3. VIBRATIONAL STUDIES OF TRANSITION METAL TRICHALCOGENIDES

3.1 Background on TMTC Lattice Dynamics

Physical properties of materials can be derived from either the electronic behaviors in a solid crystal or the movement of atoms about their equilibrium positions. These atomic vibrations (phonons) in a material generally govern its thermal properties and light-matter interactions [76]. In anisotropic materials, interactions of this sort are of particular interest due to potentially different vibrational properties seen in different crystalline axes. This chapter provides greater insight on the structure and vibrational properties of the quasi-1D transition metal trichalcogenides through a series rigorous theoretical and experimental studies.

The unique physical properties associated with transition metal trichalcogenides stem from their highly anisotropic crystal structure. Their chain-like structures and dynamics of the vibrational modes influence properties such as their optical or thermoelectric behavior. The ability to study this lattice dynamical behavior provides greater insight into the crystal structure of TMTCs in addition to better understanding how lattice vibrations affect their materials properties. Few studies have been conducted on the lattice dynamics for low dimensional anisotropic materials. Black phosphorus vibrational modes have been investigated under strained conditions [62]. Wu *et al*. began initial studies on the vibrational properties of TiS_3 nanosheets [77]. Vibrational properties for other

materials within this TMTC system have yet to be explored. The Raman spectra for bulk TiS_3, ZrS_3, and HfS_3 crystals has been previously reported [78–80]. However, the understanding of the origin of these Raman peaks and their correlation to the vibrational characteristics of TMTCs is still relatively unknown. In the following sections, theoretical studies on the lattice dynamics of TMTCs illustrate the vibrational behavior of TiS_3, ZrS_3, and HfS_3 in order to shed light on the fundamental nature of these Raman modes and how they related to the crystal structure of these materials.

Transition metal trichalcogenides typically crystallize into monoclinic structures. Each primitive unit cell contains 2 metal atoms and 6 chalcogen atoms. As previously mentioned, the atoms are arranged as a trigonal prism which can exist in either an A variant ($ZrSe_3$ type) or B variant (TiS_3 type) and extend along a single direction to form an MX_3 chain. This 8 atom primitive cell yields 24 vibrational modes which include 3 acoustic branches and 21 optical branches at the Brillouin zone center $\Gamma = 0$. A set of 8 x 3 irreducible representations for isolated chains of $p2_{1/m}$ space group symmetry can be expressed in the following:

$$\Gamma_{\text{chain}} = 4A_1 + 3B_1 + A_2 + 4B_2 \tag{3.1}$$

However, a similar representation can be found for the entire crystal structure as expressed by the following irreducible representation:

$$\Gamma_{\text{crystal}} = 4A_u + 4B_g + 8A_g + 8B_u \tag{3.2}$$

The total number of IR-active and Raman-active modes can be expressed through these representations. Based on previous reports on the selection rules derived from the

polarizability tensors associated with the irreducible representations of isolated chains and the crystal, certain modes are associated with atomic displacements parallel or perpendicular to the crystal and isolated chain direction along the b-axis. The A_u and B_g modes are parallel to the crystal direction while the A_2 and B_1 modes are parallel to the chain direction. In contrast, the A_g and B_u modes are perpendicular to the crystal direction while the A_1 and B_2 modes are perpendicular to the chain direction [81].

3.2 Theoretical Study on Phonon Dispersion

To better understand and visualize the vibrational modes of TMTCs, theoretical vibrational studies were conducted on TiS_3, ZrS_3, and HfS_3. Many of these studies make use of density functional theory (DFT) calculations and small displacement theory to calculate the phonon dispersion and atomic motions for TMTCs. Computational methods used in this study are described in the following section.

3.2.1 Computational Methodology

First principles calculations were conducted using density functional theory (DFT) as the underlying framework. Vienna Ab initio Simulation Package (VASP) was used to calculate the monolayer crystal structures of MX_3 materials [82-84]. The Perdew-Burke-Ernzerhof (PBE) form of the generalized gradient approximation (GGA) was used in order to determine the electron exchange and correlation potentials [85]. The vibrational properties and phonon dispersion were calculated for a 128-atom super cell by using the

small displacement method [86]. Phonon dispersion plots and atomic motions for individual unit cells with corresponding eigenvectors were generated for TiS_3, ZrS_3, and HfS_3 crystals.

3.2.2 Phonon Dispersion

A single primitive cell of 8 atoms contains 3 acoustic modes and 21 optical modes. Out of these optical modes, 9 modes are IR-active and the remaining 12 are Raman-active. The following phonon dispersion plots illustrate all 24 branches for each TMTC crystal. Branches that appear to be flat have a high density of states (DOS) which potentially enable a Raman-active signal to be detected during experimental measurements.

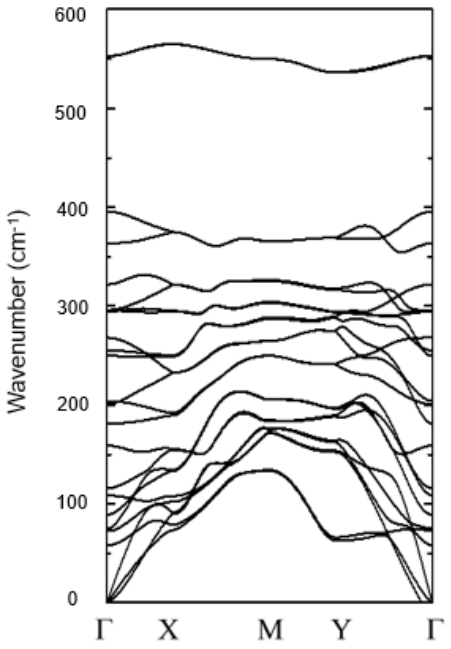

Figure 10. Phonon dispersion curves for TiS_3.

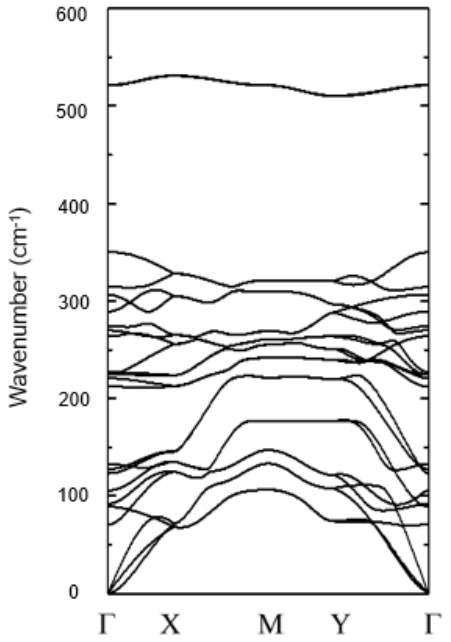

Figure 11. Phonon dispersion curves for ZrS_3.

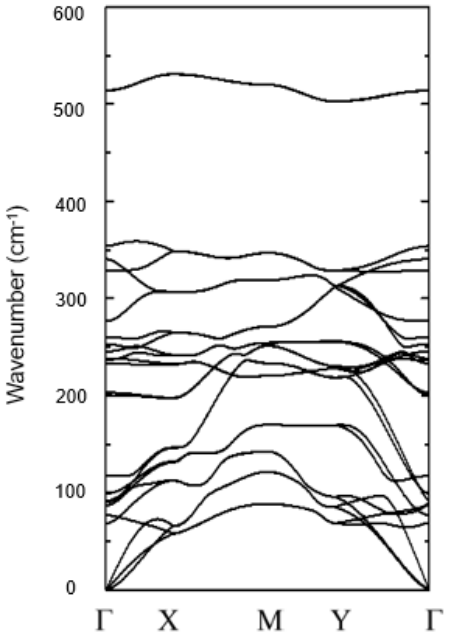

Figure 12. Phonon dispersion curves for HfS_3.

3.3 Theoretical Atomic Displacement

3.3.1 Atomic Motions for TiS_3

In the Raman spectra for TiS_3, there are four prominent peaks that illustrate four Raman-active modes. Each mode corresponds to an atomic motion of atoms in the unit cell of TiS_3 which extend along the length of the chain. Raman shows four characteristic peaks at 172, 299, 372, and 557 cm^{-1}. This matches reasonably well with the calculated phonon dispersion curves as no further 1^{st} order modes were seen beyond 600 cm^{-1}. Each peak is representative of a particular atomic displacement of a unit cell in the a-c plane with motions extending along the b-axis. For reference, the sulfur atom in a chain bonded to a metal atom in the adjacent chain will be referred to as "inner sulfur" atom and the two sulfur atoms bonded solely to the metal atom will be referred to as "outer sulfur" atom. In the low frequency mode (mode I) corresponding to 172 cm^{-1}, the metal and outer sulfur atoms are shown to be moving in the same direction out of plane for a single chain. With respect to the rotational center of the unit cell, the two sets of metal and outer sulfur atoms in adjacent chains move in opposite directions while staying in-phase. This low frequency motion is characterized as a rigid vibration. Mode II corresponds with the Raman peak at 299 cm^{-1} and shows metal and outer sulfur atoms within the same chain vibrating in opposite directions. As Wu *et al*. reported, there are two motions that correspond to this mode indicating degenerate phonon branches in mode II for TiS_3 [77]. These out of plane motions extend along the b-axis of the chain and are referred to as internal vibrations. Mode III behaves in a similar manner to mode II. However, it is the metal and inner sulfur atoms

that move in opposite directions within a single chain. The vibrations of this mode is also referred to as internal vibrations. Degenerate branches present themselves in the high frequency mode (mode IV) and are presented as two sets of atomic motions. The outer sulfur atoms in a chain vibrate laterally within the plane either towards each other in 1) and away from each other in 2). These mode IV motions are referred to as in-plane or S-S diatomic oscillations. The figure below shows a graphical representation of the atomic motions of each mode with corresponding eigenvectors that illustrate the direction of atomic motion. Red arrows indicate metal atom motion and blue arrows indicate sulfur atom motion.

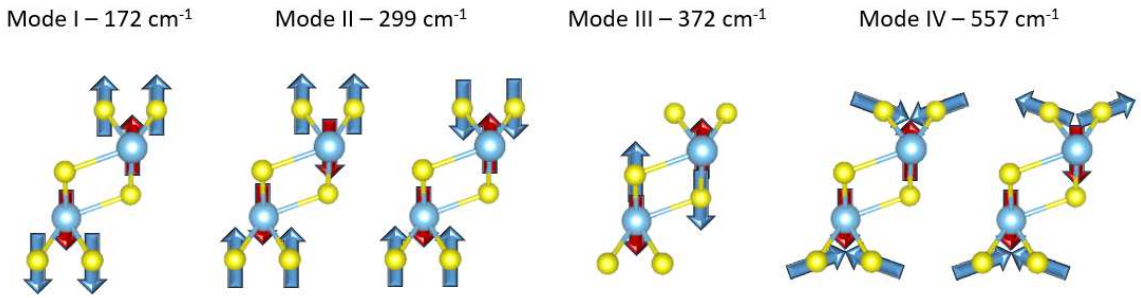

Figure 13. Atomic motions for Raman-active modes in TiS_3.

3.3.2 Atomic Motions for ZrS_3 and HfS_3

Atomic displacements for ZrS_3 and HfS_3 behave in the same manner but differ slightly from the motion displayed for TiS_3. ZrS_3 Raman spectra shows four characteristic peaks at 151, 281, 320, and 528 cm^{-1} which matches the calculated phonon dispersion. The atomic motions for each mode in ZrS_3 are the same as TiS_3 motion with the exception of

mode II where there is no degeneracy and only one motion is illustrated. Mode I is a rigid vibration. Mode II and III are internal vibrations. Mode IV is contains degenerate phonon branches and is still referred to as S-S diatomic oscillations.

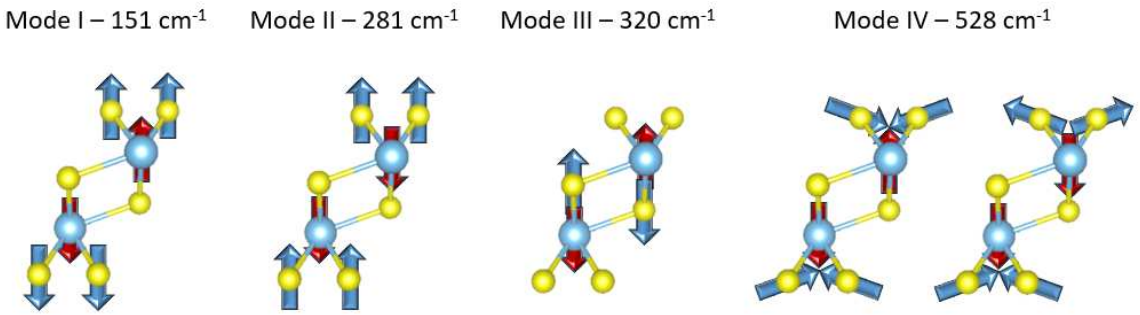

Figure 14. Atomic motions for Raman-active modes in ZrS_3.

The same conclusions can be drawn for HfS_3 as well. HfS_3 Raman spectra shows four characteristic peaks at 128, 260, 321, and 524 cm^{-1}. The motion for these atoms is the same as ZrS_3 for each mode presented. Mode I is a rigid vibration. Mode II and III are internal vibrations. Mode IV is contains degenerate phonon branches and is still referred to as S-S diatomic oscillations. Each of these modes are visualized in the figure below.

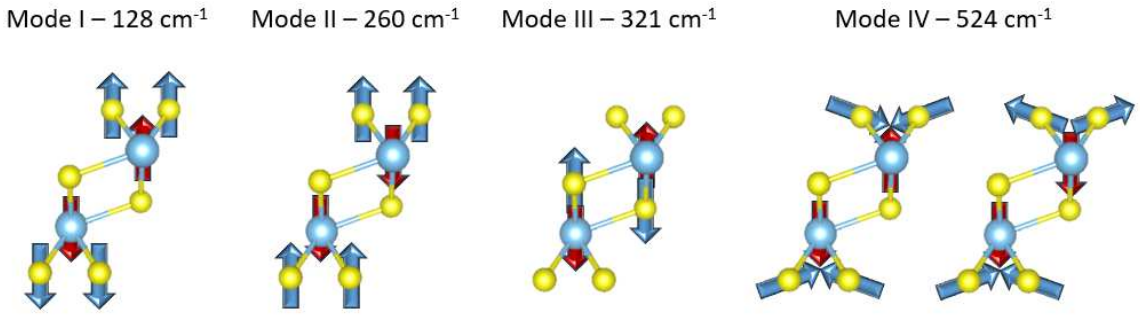

Figure 15. Atomic motions for Raman-active modes in HfS_3.

3.4 Experimental Correlation to Phonon Dispersion

The combination of theoretically calculated phonon dispersion and atomic displacements with the experimentally determined Raman spectrum of TMTC crystals provides enough information to begin understanding the vibrational nature of anisotropic TMTCs. DFT calculations have indicated the phonon branches which correspond to the prominent Raman response and at what frequencies these peaks arise from. Each TMTC crystal shows similar vibrational behavior as each of their peaks are found as similar frequencies. This is further demonstrated by the similarity of their atomic displacements. With the exception of mode II for TiS_3, the rigid-chain, internal and S-S diatomic vibrations are seen across all of the explored trichalcogenides. Through this understanding of the vibrational nature of TiS_3, ZrS_3, and HfS_3, a basis has been established for understanding the lattice dynamics of other TMTC materials.

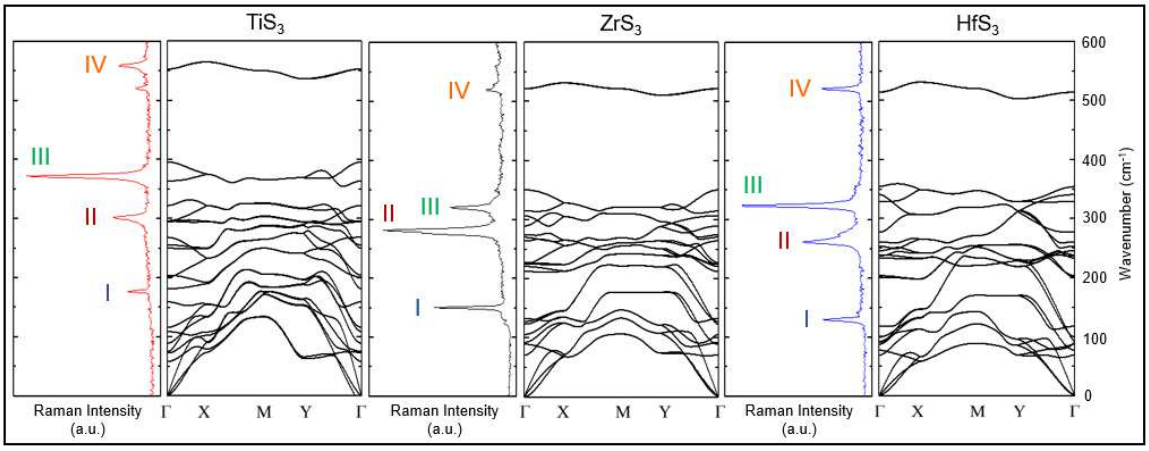

Figure 16. Comparison of theoretical phonon calculation and experimental Raman spectra.

CHAPTER 4

4. ANGLE-RESOLVED POLARIZATION OF ANISOTROPIC MATERIALS

4.1 Polarization Anisotropy of MX_3 Materials

Establishing a fundamental understanding of the vibrational characteristics of TMTCs provides insight into their other attributes such as polarizability. TMTC properties are known to be more prominent along the b-axis direction which is also the direction of anisotropy. This crystalline axis can be readily identified visually by observing the longer edge of a TMTC flake. However, it is important to note that visual inspection may not always be reliable. When exfoliating a crystal, the flake may not always cleave into a shape where the b-axis direction is clearly seen. Therefore, it is necessary to determine a non-destructive technique to readily identify the b-axis direction of a TMTC flake. A variant of Raman spectroscopy is utilized in this endeavor. Angle-resolved Raman spectroscopy takes advantage of the anisotropic polarization of TMTCs and is used as a time efficient and non-destructive optical method to determine the direction of crystalline anisotropy prior to device fabrication or other applications that require linear dichroism [70]. This chapter probes the polarization behavior of TMTCs in order to understand which Raman peaks correlate to their chain direction and if this behavior is thickness dependent.

4.1.1 Experimental Setup

The measurements for angle-resolved Raman spectroscopy were carried out in the InVia Renishaw system that was mentioned previously. The as-prepared TMTC flakes on SiO_2/Si substrates are placed onto an attachment for the microscope stage. This attachment (figure 17) magnetically attaches onto the microscope stage and contains a circular rotating platform which is numerically incremented for a 360 degree rotation.

Flakes with visibly longer edges (clear b-axis directions) were chosen for measurements. For this system, the laser polarization direction is indicated in the figure. In this position both the incident laser polarization and polarization detection directions are parallel to each other. An MX_3 flake is aligned parallel to these two directions and this position is referenced as the zero-degree position. Measurements were conducted with the laser polarization direction normal and orthogonal to the polarization detection direction in order to gain a more comprehensive insight into the polarization response for TMTCs. Normal configuration refers to the polarization excitation being parallel to the detection direction while the excitations is perpendicular to the detection direction for orthogonal configuration. The Raman response was much greater in the normal configuration instead of the orthogonal configuration so only the former was included in the scope of this work.

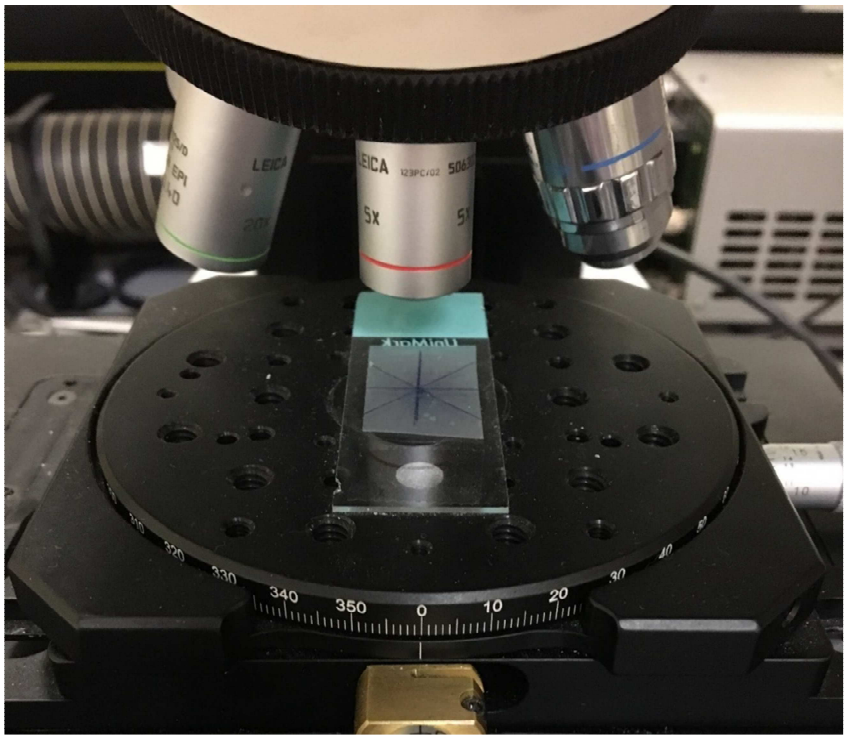

Figure 17. Rotating stage under an optical microscope for angle-resolved Raman measurements.

The first Raman measurement is made at the zero-degree position. Subsequent measurements are made by rotating the disc by an increment of 15 degrees and performing a Raman measurement on the same flake. The overall measurement is complete when a full rotation is made. Angle theta is defined as the angle between the b-axis direction of the crystal and the polarization direction with theta increasing as the flake moves away from its zero-degree position.

4.2 Anisotropic Response of MX_3 Materials

After collecting the Raman spectra at various angles of theta, the Raman intensity for the characteristic peaks changes as a function of angle. Since the b-axis direction is aligned with the polarization direction at the zero-degree position, it is postulated that the intensity for each of the characteristic Raman modes reaches its maximum value. In contrast, it is hypothesized that the peak intensities would also be at their minimum along the a-axis in this position. A closer look at the Raman spectrum for ZrS_3 at different theta values shows a variation in peak intensity not seen in many other 2D materials.

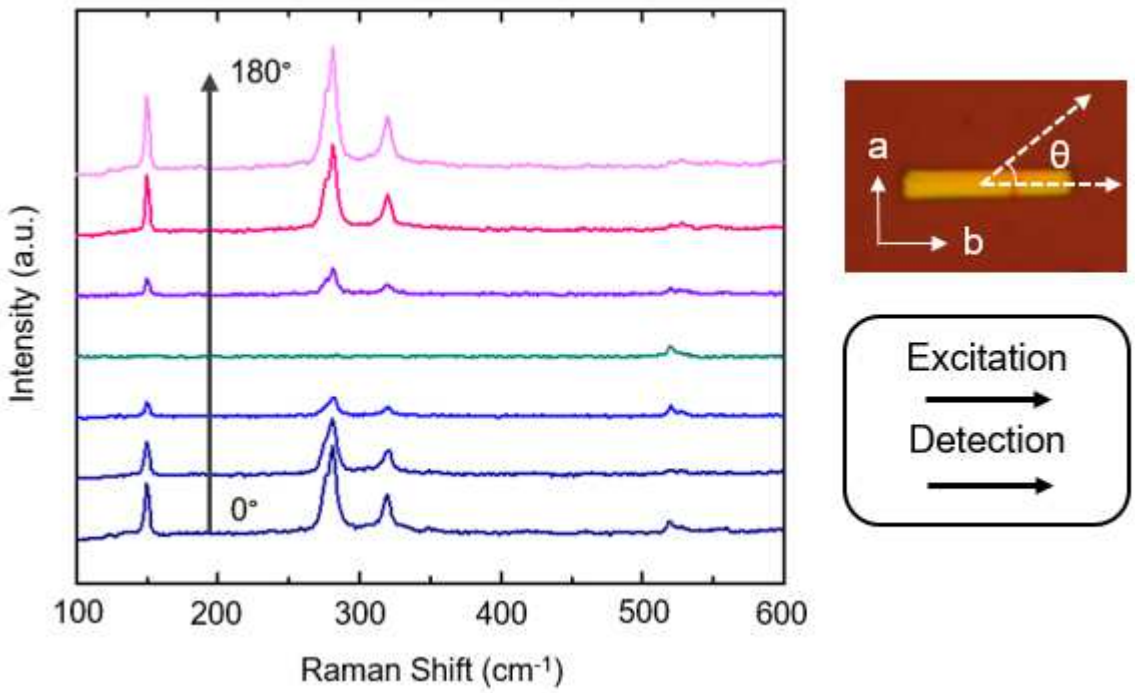

Figure 18. Raman peak intensity shift of typical MX_3 for different theta values with polarization excitation and detection directions shown.

TiS_3 and HfS_3 show the same peak intensity various at different values of theta. In order to better visualize the anisotropic response of a particular mode, polar plots are generated through plotting the maximum intensity value of a vibrational mode as a function of angle. With maximum values seen at the zero-degree position, it is expected that the optical polarization for TMTC flakes is strongest at 0° and 180° and weakest at 90° and 270°. However, this behavior is not always the case for each individual mode.

4.2.1 Polarization Response for Thick Flakes

Polar plots are generated for TiS_3, ZrS_3, and HfS_3 flakes that have a relatively large thickness (~50-100 nm). For TiS_3, the 372 cm^{-1} peak corresponding to mode III was the most prominent of the Raman-active peaks and appeared to experience the greatest sensitivity to changes in peak intensity at different theta. The mode III polar plot yields a two-lobed shape that lies parallel to the chain direction of the TiS_3 flake. The shape of this plot agrees with the earlier claim that polarization response is maximized at 0° and 180°. However, the other modes of TiS_3 do not show this type of response. Mode I is shows a two-lobe plot that is offset from the zero-degree position by approximately 90°. The plot for mode II depicts a symmetric four-lobed plot with lobe maximum values perpendicular to each other. Mode IV shows no anisotropic response, likely due to the S-S diatomic oscillations vibrating in-plane rather than out-of-plane which does not contribute to the overall crystal anisotropy.

ZrS_3 anisotropic response is far more apparent. Each of the four modes for ZrS_3 show the predicted two-lobed polar plot, each at various intensities. The strongest intensity

can be seen for mode II followed by mode I, mode III, and lastly mode IV. The S-S diatomic oscillations displays a rather weak polarization dependence for ZrS_3, thus does not provide a sufficient signal to be used for determining the crystalline orientation. HfS_3 anisotropy is quite similar to that of ZrS_3. Three of its Raman modes show a two-lobed polarization response along the zero-degree position at various intensities. Mode III is the strongest for the three modes, followed by mode II and Mode I. There is an anomaly with mode IV of HfS_3 in that it shows a strong two-lobed polarization plot in a direction perpendicular to the zero-degree position. Since mode IV involves, S-S atomic vibrations which do not contribute to the overall anisotropic response. Across the studied TMTC materials, it appears mode III vibrations is shared between each of them.

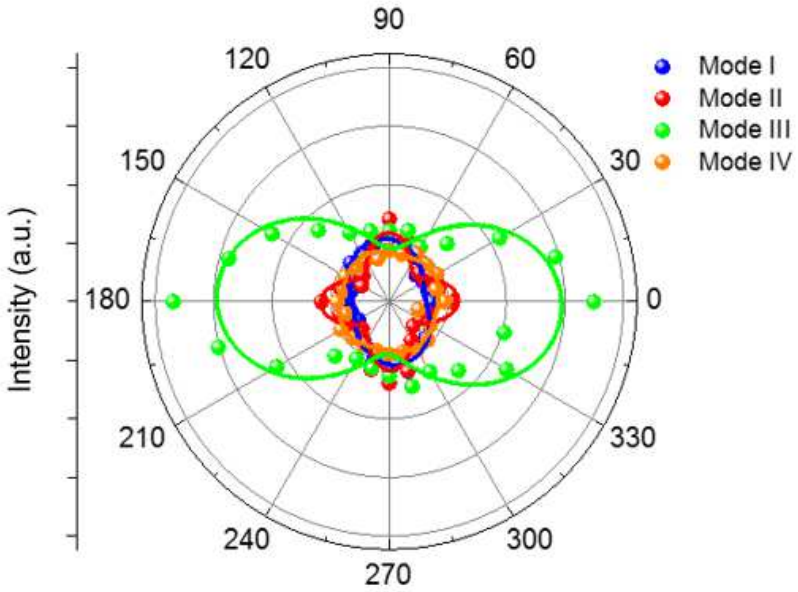

Figure 19. Polar plots for TiS_3.

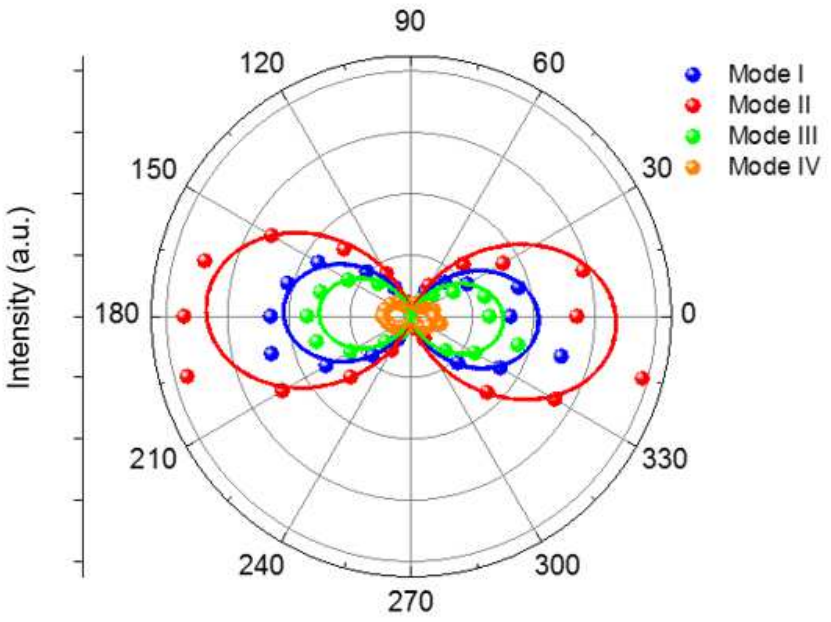

Figure 20. Polar plots for ZrS_3.

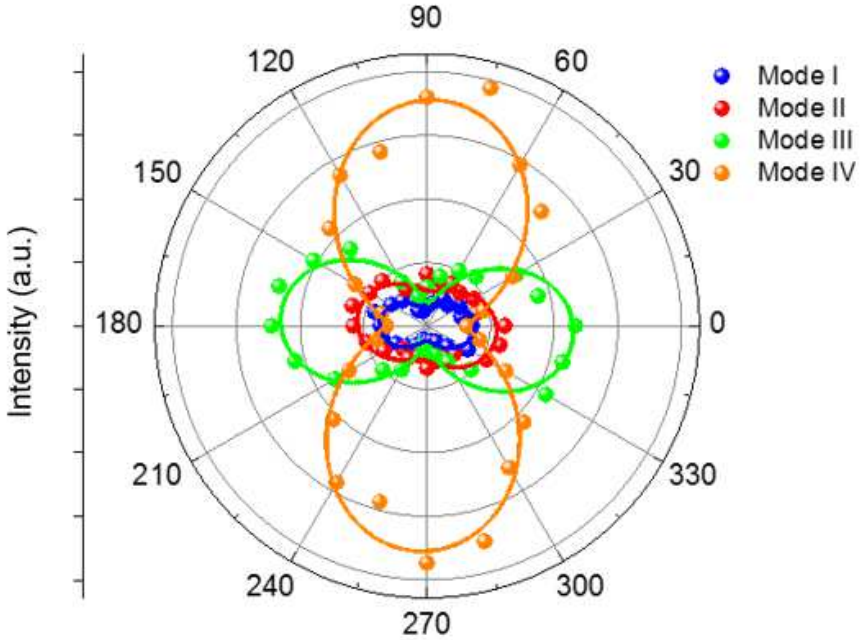

Figure 21. Polar plots for HfS_3.

4.2.2 Polarization Response for Thin Flakes

In addition to thick TMTC flakes, the same angle-resolved studies were conducted on relatively thin flakes (< 10 nm) in order to determine if the same anisotropic response can be seen and if this behavior is thickness dependent. Thin flakes less than 10 nm in thickness were identified by their dark violet contrast on the SiO_2/Si substrate. The same procedure performed on thick flakes was used to probe the polarization anisotropy for thin flakes. Flakes with the visibly longer edge were aligned parallel to the polarization excitation of the incident laser; this was referenced as the zero-degree position. Rotations of 15 degree increments were made until Raman measurements were completed for a full rotation. While flakes less than 10 nm for TiS_3 and ZrS_3 were used, an exception was made for HfS_3 thin flakes. The incident laser, even at low excitation energies, damages the thin HfS_3 flake exfoliated on SiO_2/Si substrates. The crystal was instead exfoliated onto bare silicon (111) in order to better dissipate the localized heating from the laser excitation. However, the difficulty locating a flake less than 10 nm under an optical microscope due to near transparent contrasts for thinner flakes, a ~20 nm flake for HfS_3 was utilized for this thickness study.

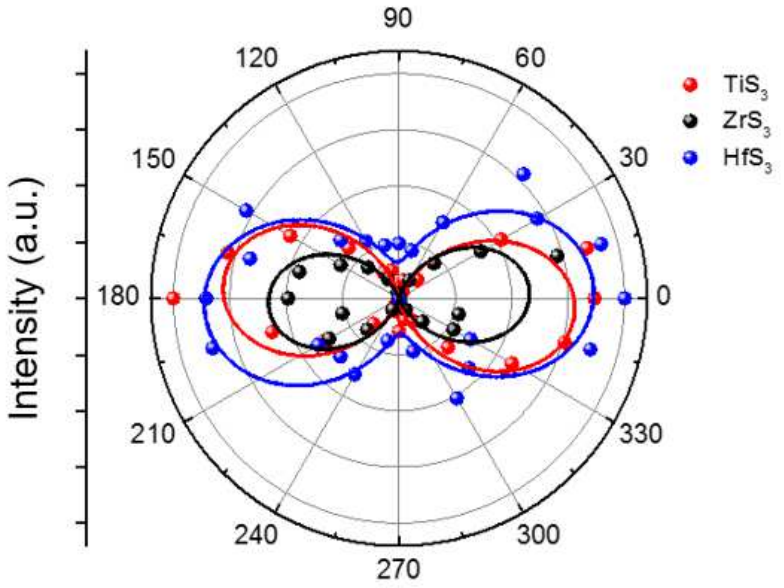

Figure 22. Polar plots for mode III vibrations of MX_3 thin crystals.

The polar plots of TiS_3, ZrS_3, and HfS_3 for thin flakes show the same behavior as plotted for thicker flakes. Each plot does not change in shape or orientation for the different modes across TMTC crystals. Again, mode III vibrations are shared between the studied thin flakes. Even at lower dimensions, the polarization anisotropy remains consistent. This reveals that polarization anisotropy is not thickness dependent.

4.3 Polarization Anisotropy Correlation to Chain Direction

Based on the previously obtained experimental data, each of the modes show various degrees of anisotropy when excited by laser light, particularly modes I-III due to their unique out-of-plane vibrations along the chain direction. Mode IV is not considered for insight into crystal anisotropy since they involve outer sulfur atoms which weakly

vibrate in-plane and do not produce a polarization response that adequately represents crystalline anisotropy. For TiS_3 only mode III shows a two-lobed polarization anisotropy along the b-axis direction. In the ZrS_3, modes I-IV each have a two-lobed polarization anisotropy with mode II having the strongest intensity. Modes I-III for HfS_3 show polarization anisotropy at various intensities along the b-axis direction. Mode IV for this system deviates from the expected response. In general, mode III shows the same behavior across all studied TMTC crystals. This mode can be reliably used to identify the b-axis direction of TMTCs due to the common out-of-plane internal vibrations that they commonly share. Angle-resolved Raman spectroscopy provides a non-destructive technique to identify the anisotropic structural properties of various TMTC materials which can potentially be extended to other anisotropic materials.

CHAPTER 5

5. POLARIZATION RESPONSE FOR TMTC ALLOYS

5.1 Alloying of 2D Materials

Two-dimensional alloys are explored as an additional method to further tune their electronic and optical properties. $Mo_xW_{1-x}Se_2$ and MoS_xSe_{1-x} are transition metal dichalcogenide solid solution alloys with band gap energies that can be tuned by varying the composition of metal or chalcogenide constituents [48,51,87,88]. Modification of band gaps in alloys leads to a greater versatility of applications in photonics. Substitutions of other metal atoms in transition metal trichalcogenides can introduce point defects which serve as phonon scattering centers [89]. The alloying of anisotropic materials is still at a seminal stage with few alloys currently synthesized. Recently, researchers have created a solid solution of $Ti_{1-x}Nb_xS_3$ for the purposes of obtaining tunable thermoelectric materials [90].

5.2 $Nb_{0.5}Ti_{0.5}S_3$

Established results for TMTC materials demonstrate properties dependent on their anisotropic crystal structure. TMTC alloys that contain extended defects could potentially distort these properties. Previously demonstrated optical techniques have been used to probe the crystal anisotropy of TMTC crystal and but have not been conducted for alloy

materials. To this end, $Ti_xNb_{1-x}S_3$ with x = 0.5 has been synthesized in order to test the applicability of angle-resolved Raman spectroscopy on for determining the primary chain directions for TMTC alloys and to probe their Raman behavior.

5.2.1 Crystal Growth

$Nb_{0.5}Ti_{0.5}S_3$ was synthesized using chemical vapor transport (CVT) in the same manner as the other MX_3 materials, specifically with similar conditions to TiS_3 growth. Niobium (Nb) and titanium (Ti) sheets were placed into a quartz ampoule with excess sulfur pellets. The ratio of Nb and Ti was kept 1:1 while the overall stoichiometric ratio for metal-sulfur precursor material remained at 1:3. The ampoule was evacuated to 10^{-6} Torr and placed into a two-zone horizontal tube furnace for growth to occur. A growth temperature of 550 °C was used for this alloy and maintained for a period of 3 days before naturally cooling to room temperature. The needle-like crystals grown on the inner walls of the quartz ampoule assume a grey hue similar to TiS_3 (figure 23).

Figure 23. $Nb_{0.5}Ti_{0.5}S_3$ crystals grown on the inner walls of a quartz ampoule.

5.3 Angle-Resolved Raman Spectroscopy

Previously, it has been demonstrated for other MX_3 materials that the polarization direction is strongest along the b-axis chain direction. Solid solution TMTC alloys containing extended defects or random crystalline structures may present challenges when identifying their anisotropic directions. CVD grown anisotropic materials such as ReS_2 and $ReSe_2$ have been shown to possess a large number of defect sites or grain boundaries which tend to randomize the chain directions within domains of this material. A reduction in long range symmetry for anisotropic materials can pose a problem for properly identifying their primary chain directions. While angle-resolved Raman spectroscopy has been proven to provide adequate information about the crystal structure of TMTCs, it remains to be seen if the same information can be obtained for a TMTC alloy.

5.3.1 Experimental Setup

The exfoliated crystals on SiO_2/Si substrates were placed on the rotating stage with the longer flake edge aligned parallel to the polarization direction of incident laser light (zero-degree position). A standard Raman spectrum for the $Nb_{0.5}Ti_{0.5}S_3$ was obtained prior to angle-resolved measurements. The angle-resolved measurements were carried out in the same manner as with previous MX_3 crystals. Polar plots for each Raman mode were generated for a full rotation of the flake.

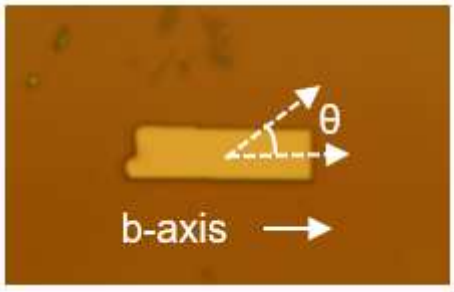

Figure 24. $Nb_{0.5}Ti_{0.5}S_3$ flake oriented in the zero-degree position.

5.3.2 Experimental Results

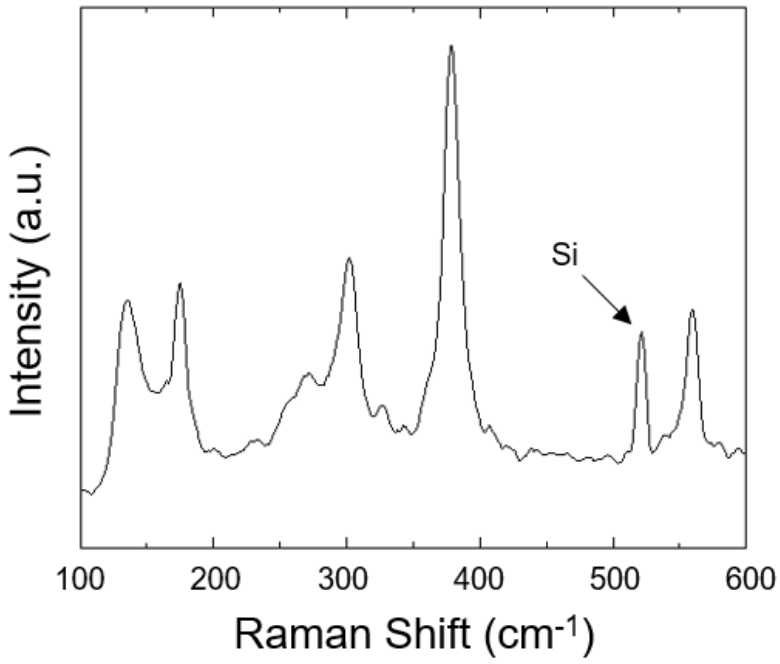

Figure 25. Raman spectra of $Nb_{0.5}Ti_{0.5}S_3$ with the silicon peak indicated.

Five prominent and sharp Raman peaks with a full-width half maximum of 5-6 were observed for $Nb_{0.5}Ti_{0.5}S_3$ which indicate a crystalline structure (figure 25). This spectrum shares similarities to crystalline TiS_3 with slight variations in several peak positions. The low frequency mode at 137 cm^{-1} show a weak two-lobed polar plot parallel to the presumed b-axis direction. Modes found at 301 and 386 cm^{-1}, however, deviate from this trend with four-lobed symmetric plots that show maximum values at 0, 90, 180, and 270 degrees. Lastly, modes found at 168 and 561 cm^{-1} show strong two-lobed plots with maximum intensity values found at 90 and 270 degrees. Based on prior definitions of crystalline anisotropy identified through mode III internal chain vibrations, this behavior is not clearly evident in $Nb_{0.5}Ti_{0.5}S_3$. None of the observed modes correspond to the b-axis

direction of $Nb_{0.5}Ti_{0.5}S_3$, with the low frequency mode at 137 cm^{-1} being an exception. However, this mode cannot be representative of the characteristic mode used to identify the chain directions for this alloy since previous studies show low frequency modes as rigid internal vibrations. Therefore, it is demonstrated that angle-resolved Raman spectroscopy cannot reasonably determine the anisotropic chain direction for this particular alloy.

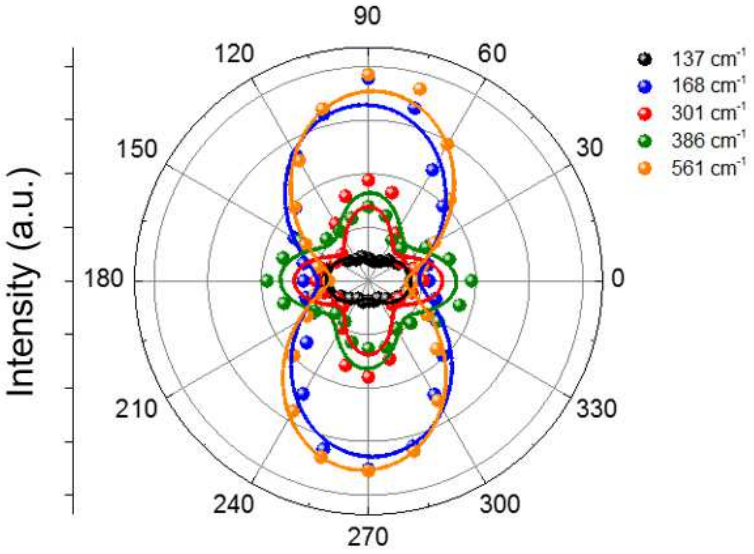

Figure 26. Polar plots for $Nb_{0.5}Ti_{0.5}S_3$ Raman modes.

5.4 Effect of Alloying on Anisotropy

The use of angle-resolved Raman spectroscopy for anisotropic materials that possess extended defects provides little information regarding the characteristic vibrational modes. The randomly oriented plots generated for each Raman mode did not provide an adequate indicator of the unique vibrational mode that is representative of the chain direction for the alloy. Such complex polar plots are likely related to the complex Raman

tensor belonging to this alloy which prevents the use of simple optical techniques to quickly identify the anisotropic chain directions. Further research on alloys of TMTCs can provide additional insight on how extended defects can affect the overall anisotropic polarization of the material. Currently, few studies have been conducted on TMTC alloys. Creating new TMTC alloys with varying compositions or combinations of transition metals or chalogens can allow for a greater extension of tunable TMTC properties. DFT calculations on alloys could potentially shed light on the behavior of alloy vibrational modes and how they differ from non-alloy species. HRSTEM studies would provide greater insight into the atomic orientation of TMTC chains or potential defect sites and how these affect the anisotropy. Because it is still not fully understood why the anisotropy is lost in TMTC alloys, additional studies are needed to better understand the Raman tensors of these materials.

CHAPTER 6

6. CONCLUSIONS AND OUTLOOK

6.1 Summary of Results

In this work, the vibrational properties of CVT grown quasi-1D transition metal trichalcogenides (TiS_3, ZrS_3, and HfS_3) has been carefully investigated through density functional theory and angle-resolved Raman spectroscopy to have a more clear understanding of the anisotropic nature of these materials. TMTC nanosheets were prepared through a mechanical exfoliation of crystals onto SiO_2/Si substrates. XRD, AFM, and Raman spectroscopy were used to characterize their crystallinity, thickness, and chemical signature respectively. DFT calculations provided the phonon dispersion and atomic motions for Raman-active modes of TMTC materials. Angle-resolved Raman spectroscopy demonstrates a polarization angle dependence on TMTC flakes with respect to the polarization direction. The b-axis direction is directly correlated with mode III vibrations which are seen across all TMTC crystals. This behavior is insensitive to the thickness of these materials. A new TMTC alloy, $Nb_{0.5}Ti_{0.5}S_3$, was synthesized through CVT and angle-resolved Raman spectroscopy was used to determine vibrational modes corresponding to anisotropy direction.

6.2 Conclusions

These results show a comprehensive overview of the fundamental origin of the vibrational modes which give rise to the characteristic Raman peaks of TMTCs. In particular, the strong out-of-plane motion of atoms along the chain direction (b-axis) is maximized when monochromatic light polarizes along the anisotropic direction of the crystal. This is readily shown through angle-resolved Raman spectroscopy as it provides a quick and non-destructive method to probe the anisotropic structure of TMTCs and illustrating the direction dependence on polarization. Additionally, this behavior is preserved even at low dimensions and is insensitive to the thickness of the material. These techniques are also used for TMTC alloys which demonstrate changes in anisotropy due to potential defects and randomized chain orientations due to alloying. Being able to comprehend the vibrational properties of TMTCs and how to identify their anisotropic directions is necessary for a further understanding of their thermal, electronic, and optical behavior which influences their use in future device applications.

6.2 Future Work

1. Despite the unique properties found in different 2D materials (both isotropic and anisotropic), a fundamental limitation of their use in device applications is the ability to synthesize them in a large scale. Being able to grow anisotropic materials using chemical vapor deposition (CVD), physical vapor deposition (PVD), or

molecular beam epitaxy (MBE) will allow these materials to be more readily used for optoelectronics, sensing technologies, or direction dependent polarization.

2. Ultimately, synthesis and understanding of these materials will lead to the fabrication of a larger array of devices and electronics. Work has been done on TiS_3-based field effect transistors [91]. These quasi-1D materials could potentially be used in sensing devices for biological or chemical applications.
3. Additional work on TMTC alloying would enable a wider range of tunable anisotropic materials. Careful characterization studies on defects of these alloys through HRSTEM, angle-resolved Raman spectroscopy, and conductive atomic force microscopy (cAFM) can lead to a better understanding on how alloying affects the anisotropic behavior of these materials.

REFERENCES

1. Novoselov, K. S., Jiang, D., Schedin, F., Booth, T. J., Khotkevich, V. V., Morozov, S. V., & Geim, A. K. (2005). Two-dimensional atomic crystals. *Proceedings of the National Academy of Sciences of the United States of America*, *102*(30), 10451-10453.

2. Mas-Balleste, R., Gomez-Navarro, C., Gomez-Herrero, J., & Zamora, F. (2011). 2D materials: to graphene and beyond. *Nanoscale*, *3*(1), 20-30.

3. Li, H., Lu, G., Wang, Y., Yin, Z., Cong, C., He, Q., ... & Zhang, H. (2013). Mechanical Exfoliation and Characterization of Single-and Few-Layer Nanosheets of WSe2, TaS2, and TaSe2. *Small*, *9*(11), 1974-1981.

4. Yi, M., & Shen, Z. (2015). A review on mechanical exfoliation for the scalable production of graphene. *Journal of Materials Chemistry A*, *3*(22), 11700-11715.

5. Coleman, J. N., Lotya, M., O'Neill, A., Bergin, S. D., King, P. J., Khan, U., ... & Shvets, I. V. (2011). Two-dimensional nanosheets produced by liquid exfoliation of layered materials. *Science*, *331*(6017), 568-571.

6. Nicolosi, V., Chhowalla, M., Kanatzidis, M. G., Strano, M. S., & Coleman, J. N. (2013). Liquid exfoliation of layered materials. *Science*, *340*(6139), 1226419.

7. Fang, H., Chuang, S., Chang, T. C., Takei, K., Takahashi, T., & Javey, A. (2012). High-performance single layered WSe2 p-FETs with chemically doped contacts. *Nano letters*, *12*(7), 3788-3792.

8. Wang, X., & Xia, F. (2015). Van der Waals heterostructures: stacked 2D materials shed light. *Nature materials*, *14*(3), 264-265.

9. Lee, Y. H., Zhang, X. Q., Zhang, W., Chang, M. T., Lin, C. T., Chang, K. D., ... & Lin, T. W. (2012). Synthesis of Large-Area MoS2 Atomic Layers with Chemical Vapor Deposition. *Advanced Materials*, *24*(17), 2320-2325.

10. Muratore, C., Hu, J. J., Wang, B., Haque, M. A., Bultman, J. E., Jespersen, M. L., ... & Voevodin, A. A. (2014). Continuous ultra-thin MoS2 films grown by low-temperature physical vapor deposition. *Applied Physics Letters*, *104*(26), 261604.

11. Vishwanath, S., Liu, X., Rouvimov, S., Mende, P. C., Azcatl, A., McDonnell, S., ... & Xing, H. G. (2015). Comprehensive structural and optical characterization of MBE grown MoSe2 on graphite, CaF2 and graphene. *2D Materials*, *2*(2), 024007.

12. Wang, Q. H., Kalantar-Zadeh, K., Kis, A., Coleman, J. N., & Strano, M. S. (2012). Electronics and optoelectronics of two-dimensional transition metal dichalcogenides. *Nature nanotechnology*, *7*(11), 699-712.

13. Geim, A. K., & Novoselov, K. S. (2007). The rise of graphene. *Nature materials*, *6*(3), 183-191.

14. Bonaccorso, F., Sun, Z., Hasan, T., & Ferrari, A. C. (2010). Graphene photonics and optoelectronics. *Nature photonics*, *4*(9), 611-622.

15. Pumera, M. (2011). Graphene-based nanomaterials for energy storage. *Energy & Environmental Science*, *4*(3), 668-674.

16. Siochi, E. J. (2014). Graphene in the sky and beyond. *Nature nanotechnology*, *9*(10), 745-747.

17. Takada, K., Sakurai, H., Takayama-Muromachi, E., Izumi, F., Dilanian, R. A., & Sasaki, T. (2003). Superconductivity in two-dimensional CoO2 layers. *Nature*, *422*(6927), 53-55.

18. Watanabe, K., Taniguchi, T., & Kanda, H. (2004). Direct-bandgap properties and evidence for ultraviolet lasing of hexagonal boron nitride single crystal. *Nature materials*, *3*(6), 404-409.

19. Dean, C. R., Young, A. F., Meric, I., Lee, C., Wang, L., Sorgenfrei, S., ... & Hone, J. (2010). Boron nitride substrates for high-quality graphene electronics. *Nature nanotechnology*, *5*(10), 722-726.

20. Giovannetti, G., Khomyakov, P. A., Brocks, G., Kelly, P. J., & Van Den Brink, J. (2007). Substrate-induced band gap in graphene on hexagonal boron nitride: Ab initio density functional calculations. *Physical Review B*, *76*(7), 073103.

21. Splendiani, A., Sun, L., Zhang, Y., Li, T., Kim, J., Chim, C. Y., ... & Wang, F. (2010). Emerging photoluminescence in monolayer MoS2. *Nano letters*, *10*(4), 1271-1275.

22. Gong, Y., Lin, J., Wang, X., Shi, G., Lei, S., Lin, Z., ... & Terrones, H. (2014). Vertical and in-plane heterostructures from WS2/MoS2 monolayers. *Nature materials*, *13*(12), 1135-1142.

23. Jariwala, D., Sangwan, V. K., Lauhon, L. J., Marks, T. J., & Hersam, M. C. (2014). Emerging device applications for semiconducting two-dimensional transition metal dichalcogenides. *ACS nano*, *8*(2), 1102-1120.

24. Balendhran, S., Walia, S., Nili, H., Sriram, S., & Bhaskaran, M. (2015). Elemental analogues of graphene: silicene, germanene, stanene, and phosphorene. *Small*, *11*(6), 640-652.

25. Zhou, X., Cheng, J., Zhou, Y., Cao, T., Hong, H., Liao, Z., ... & Yu, D. (2015). Strong second-harmonic generation in atomic layered GaSe. *Journal of the American Chemical Society*, *137*(25), 7994-7997.

26. Sánchez-Royo, J. F., Muñoz-Matutano, G., Brotons-Gisbert, M., Martínez-Pastor, J. P., Segura, A., Cantarero, A., ... & Marqués-Hueso, J. (2014). Electronic structure, optical properties, and lattice dynamics in atomically thin indium selenide flakes. *Nano Research*, *7*(10), 1556-1568.

27. Brotons-Gisbert, M., Andres-Penares, D., Suh, J., Hidalgo, F., Abargues, R., Rodríguez-Cantó, P. J., ... & Ordejón, P. (2016). Nanotexturing to enhance photoluminescent response of atomically thin indium selenide with highly tunable band gap. *Nano Lett*, *16*, 3221-3229.

28. Li, X., Basile, L., Yoon, M., Ma, C., Puretzky, A. A., Lee, J., ... & Xiao, K. (2015). Revealing the Preferred Interlayer Orientations and Stackings of Two-Dimensional Bilayer Gallium Selenide Crystals. *Angewandte Chemie International Edition*, *54*(9), 2712-2717.

29. Zhou, Y., Nie, Y., Liu, Y., Yan, K., Hong, J., Jin, C., ... & Peng, H. (2014). Epitaxy and photoresponse of two-dimensional GaSe crystals on flexible transparent mica sheets. *Acs Nano*, *8*(2), 1485-1490.

30. Tongay, S., Sahin, H., Ko, C., Luce, A., Fan, W., Liu, K., ... & Ogletree, D. F. (2014). Monolayer behaviour in bulk ReS2 due to electronic and vibrational decoupling. *Nature communications*, *5, 3252*.

31. Chenet, D. A., Aslan, O. B., Huang, P. Y., Fan, C., van der Zande, A. M., Heinz, T. F., & Hone, J. C. (2015). In-plane anisotropy in mono-and few-layer ReS2 probed by Raman spectroscopy and scanning transmission electron microscopy. *Nano letters*, *15*(9), 5667-5672.

32. Lin, Y. C., Komsa, H. P., Yeh, C. H., Bjorkman, T., Liang, Z. Y., Ho, C. H., ... & Suenaga, K. (2015). Single-layer ReS2: two-dimensional semiconductor with tunable in-plane anisotropy. *ACS nano*, *9*(11), 11249-11257.

33. Wolverson, D., Crampin, S., Kazemi, A. S., Ilie, A., & Bending, S. J. (2014). Raman spectra of monolayer, few-layer, and bulk ReSe2: an anisotropic layered semiconductor. *ACS nano*, *8*(11), 11154-11164.

34. Hart, L., Dale, S., Hoye, S., Webb, J. L., & Wolverson, D. (2016). Rhenium dichalcogenides: layered semiconductors with two vertical orientations. *Nano letters*, *16*(2), 1381-1386.

35. Colson, J. W., Mann, J. A., DeBlase, C. R., & Dichtel, W. R. (2015). Patterned growth of oriented 2D covalent organic framework thin films on single-layer graphene. *Journal of Polymer Science Part A: Polymer Chemistry*, *53*(2), 378-384.

36. Lee, C., Wei, X., Kysar, J. W., & Hone, J. (2008). Measurement of the elastic properties and intrinsic strength of monolayer graphene. *Science*, *321*(5887), 385-388.

37. Bunch, J. S., Verbridge, S. S., Alden, J. S., Van Der Zande, A. M., Parpia, J. M., Craighead, H. G., & McEuen, P. L. (2008). Impermeable atomic membranes from graphene sheets. *Nano letters*, *8*(8), 2458-2462.

38. Nair, R. R., Blake, P., Grigorenko, A. N., Novoselov, K. S., Booth, T. J., Stauber, T., ... & Geim, A. K. (2008). Fine structure constant defines visual transparency of graphene. *Science*, *320*(5881), 1308-1308.

39. Liu, C., Yu, Z., Neff, D., Zhamu, A., & Jang, B. Z. (2010). Graphene-based supercapacitor with an ultrahigh energy density. *Nano letters*, *10*(12), 4863-4868.

40. Han, Y., Xu, Z., & Gao, C. (2013). Ultrathin graphene nanofiltration membrane for water purification. *Advanced Functional Materials*, *23*(29), 3693-3700.

41. Sprinkle, M., Siegel, D., Hu, Y., Hicks, J., Tejeda, A., Taleb-Ibrahimi, A., ... & Chiang, S. (2009). First direct observation of a nearly ideal graphene band structure. *Physical review letters*, *103*(22), 226803.

42. Novoselov, K. S., Geim, A. K., Morozov, S., Jiang, D., Katsnelson, M., Grigorieva, I., ... & Firsov, A. (2005). Two-dimensional gas of massless Dirac fermions in graphene. *nature*, *438*(7065), 197-200.

43. Ni, Z. H., Yu, T., Lu, Y. H., Wang, Y. Y., Feng, Y. P., & Shen, Z. X. (2008). Uniaxial strain on graphene: Raman spectroscopy study and band-gap opening. *ACS nano*, *2*(11), 2301-2305.

44. Sun, L., Li, Q., Ren, H., Su, H., Shi, Q. W., & Yang, J. (2008). Strain effect on electronic structures of graphene nanoribbons: A first-principles study. *The Journal of chemical physics*, *129*(7), 074704.

45. Ramakrishna Matte, H. S. S., Gomathi, A., Manna, A. K., Late, D. J., Datta, R., Pati, S. K., & Rao, C. N. R. (2010). MoS2 and WS2 analogues of graphene. *Angewandte Chemie*, *122*(24), 4153-4156.

46. Lee, G. H., Yu, Y. J., Cui, X., Petrone, N., Lee, C. H., Choi, M. S., ... & Taniguchi, T. (2013). Flexible and transparent MoS2 field-effect transistors on hexagonal boron nitride-graphene heterostructures. *ACS nano*, *7*(9), 7931-7936.

47. Zhou, W., Zou, X., Najmaei, S., Liu, Z., Shi, Y., Kong, J., ... & Idrobo, J. C. (2013). Intrinsic structural defects in monolayer molybdenum disulfide. *Nano letters*, *13*(6), 2615-2622.

48. Komsa, H. P., & Krasheninnikov, A. V. (2012). Two-dimensional transition metal dichalcogenide alloys: stability and electronic properties. *The journal of physical chemistry letters*, *3*(23), 3652-3656.

49. Yang, S., Wang, C., Ataca, C., Li, Y., Chen, H., Cai, H., ... & Tongay, S. (2016). Self-Driven Photodetector and Ambipolar Transistor in Atomically Thin GaTe-MoS2 p–n vdW Heterostructure. *ACS applied materials & interfaces*, *8*(4), 2533-2539.

50. Wang, H., Tsai, C., Kong, D., Chan, K., Abild-Pedersen, F., Nørskov, J. K., & Cui, Y. (2015). Transition-metal doped edge sites in vertically aligned MoS2 catalysts for enhanced hydrogen evolution. *Nano Research*, *8*(2), 566-575.

51. Gong, Q., Sheng, S., Ye, H., Han, N., Cheng, L., & Li, Y. (2016). MoxW1− x (SySe1− y) 2 Alloy Nanoflakes for High-Performance Electrocatalytic Hydrogen Evolution. *Particle & Particle Systems Characterization*, *33*(8), 576-582.

52. Tsai, M. L., Su, S. H., Chang, J. K., Tsai, D. S., Chen, C. H., Wu, C. I., ... & He, J. H. (2014). Monolayer MoS2 heterojunction solar cells. *Acs Nano*, *8*(8), 8317-8322.

53. Sarkar, D., Liu, W., Xie, X., Anselmo, A. C., Mitragotri, S., & Banerjee, K. (2014). MoS2 field-effect transistor for next-generation label-free biosensors. *ACS nano*, *8*(4), 3992-4003.

54. Zeng, H., Dai, J., Yao, W., Xiao, D., & Cui, X. (2012). Valley polarization in MoS2 monolayers by optical pumping. *Nature nanotechnology*, *7*(8), 490-493.

55. Mudd, G. W., Molas, M. R., Chen, X., Zólyomi, V., Nogajewski, K., Kudrynskyi, Z. R., ... & Potemski, M. (2016). The direct-to-indirect band gap crossover in two-dimensional van der Waals Indium Selenide crystals. *Scientific Reports*, *6, 39619*.

56. Cai, H., Kang, J., Sahin, H., Chen, B., Suslu, A., Wu, K., ... & Tongay, S. (2016). Exciton pumping across type-I gallium chalcogenide heterojunctions. *Nanotechnology*, *27*(6), 065203.

57. Cai, H., Soignard, E., Ataca, C., Chen, B., Ko, C., Aoki, T., ... & Ogletree, F. D. (2016). Band Engineering by Controlling vdW Epitaxy Growth Mode in 2D Gallium Chalcogenides. *Advanced Materials*, *28*(34), 7375-7382.

58. Bandurin, D. A., Tyurnina, A. V., Geliang, L. Y., Mishchenko, A., Zólyomi, V., Morozov, S. V., ... & Kovalyuk, Z. D. (2016). High electron mobility, quantum Hall effect and anomalous optical response in atomically thin InSe. *Nature Nanotechnology, 12, 223-227*.

59. Chen, Z., Biscaras, J., & Shukla, A. (2015). A high performance graphene/few-layer InSe photo-detector. *Nanoscale*, *7*(14), 5981-5986.

60. Ling, X., Wang, H., Huang, S., Xia, F., & Dresselhaus, M. S. (2015). The renaissance of black phosphorus. *Proceedings of the National Academy of Sciences*, *112*(15), 4523-4530.

61. Liu, H., Neal, A. T., Zhu, Z., Xu, X., Tomanek, D., Ye, P. D., & Luo, Z. (2014). Phosphorene: an unexplored 2D semiconductor with a high hole mobility. *ACS nano, 8, 4033-4041*.

62. Xia, F., Wang, H., & Jia, Y. (2014). Rediscovering black phosphorus as an anisotropic layered material for optoelectronics and electronics. *Nature communications*, *5, 4458*.

63. Lee, S., Yang, F., Suh, J., Yang, S., Lee, Y., Li, G., ... & Park, J. (2015). Anisotropic in-plane thermal conductivity of black phosphorus nanoribbons at temperatures higher than 100 [thinsp] K. *Nature communications*, *6*.

64. Wu, K., Chen, B., Yang, S., Wang, G., Kong, W., Cai, H., ... & Suslu, A. (2016). Domain architectures and grain boundaries in chemical vapor deposited highly anisotropic ReS2 monolayer films. *Nano Letters*, *16*(9), 5888-5894.

65. Cai, H., Chen, B., Wang, G., Soignard, E., Khosravi, A., Manca, M., ... & Tongay, S. (2017). Synthesis of Highly Anisotropic Semiconducting GaTe Nanomaterials and Emerging Properties Enabled by Epitaxy. *Advanced Materials*, *29*(8).

66. Huang, S., Tatsumi, Y., Ling, X., Guo, H., Wang, Z., Watson, G., ... & Yang, T. (2016). In-plane optical anisotropy of layered gallium telluride. *ACS nano*, *10*(9), 8964-8972.

67. Furuseth, S. I. G. R. I. D., Brattas, L., & Kjekshus, A. (1975). Crystal Structures of TiS 3, ZrS 3, ZrSe 3, ZrTe 3, HfS 3 and HfSe 3. *Acta Chemica Scandinavica*, *29*, 623.

68. Guilmeau, E., Berthebaud, D., Misse, P. R., Hébert, S., Lebedev, O. I., Chateigner, D., ... & Maignan, A. (2014). ZrSe3-Type variant of TiS3: Structure and thermoelectric properties. *Chemistry of Materials*, *26*(19), 5585-5591.

69. Island, J. O., Barawi, M., Biele, R., Almazán, A., Clamagirand, J. M., Ares, J. R., ... & Ferrer, I. J. (2015). TiS3 transistors with tailored morphology and electrical properties. *Advanced Materials*, *27*(16), 2595-2601.

70. Pant, A., Torun, E., Chen, B., Bhat, S., Fan, X., Wu, K., ... & Tongay, S. (2016). Strong dichroic emission in the pseudo one dimensional material ZrS 3. *Nanoscale*, *8*(36), 16259-16265.

71. Li, M., Dai, J., & Zeng, X. C. (2015). Tuning the electronic properties of transition-metal trichalcogenides via tensile strain. *Nanoscale*, *7*(37), 15385-15391.

72. Levy, F., & Berger, H. (1983). Single crystals of transition metal trichalcogenides. *Journal of Crystal Growth*, *61*(1), 61-68.

73. Ubaldini, A., Jacimovic, J., Ubrig, N., & Giannini, E. (2013). Chloride-driven chemical vapor transport method for crystal growth of transition metal dichalcogenides. *Crystal Growth & Design*, *13*(10), 4453-4459

74. Late, D. J., Liu, B., Matte, H. S. S., Rao, C. N. R., & Dravid, V. P. (2012). Rapid characterization of ultrathin layers of chalcogenides on SiO2/Si substrates. *Advanced Functional Materials*, *22*(9), 1894-1905.

75. Ferrari, A. C., & Basko, D. M. (2013). Raman spectroscopy as a versatile tool for studying the properties of graphene. *Nature nanotechnology*, *8*(4), 235-246.

76. Lienau, C., Noginov, M. A., Lončar, M., Bauer, C., & Giessen, H. (2014). Light–matter interactions at the nanoscale. *Journal of Optics*, *16*(11), 110201.

77. Wu, K., Torun, E., Sahin, H., Chen, B., Fan, X., Pant, A., ... & Tongay, S. (2016). Unusual lattice vibration characteristics in whiskers of the pseudo-one-dimensional titanium trisulfide TiS3. *Nature Communications*, *7*.

78. Cavellin, C. D., & Jandl, S. (1980). Raman spectra of HfS3. *Solid State Communications*, *33*(7), 813-816.

79. Jandl, S., Cavellin, C. D., & Harbec, J. Y. (1979). Raman spectra of ZrS3. *Solid State Communications*, *31*(5), 351-353.

80. Island, J. O., Biele, R., Barawi, M., Clamagirand, J. M., Ares, J. R., Sánchez, C., ... & Castellanos-Gomez, A. (2016). Titanium trisulfide (TiS3): a 2D semiconductor with quasi-1D optical and electronic properties. *Scientific reports*, *6, 22214*.

81. Wieting, T. J., Grisel, A., & Levy, F. (1981). Lattice dynamical study of the low-dimensional type B compounds TiS3, HfSe3 and ZrTe3. *Physica B+ C*, *105*(1-3), 366-369.

82. Kresse, G., & Hafner, J. (1993). Ab initio molecular dynamics for liquid metals. *Physical Review B*, *47*(1), 558.

83. Kresse, G., & Furthmüller, J. (1996). Efficient iterative schemes for ab initio total-energy calculations using a plane-wave basis set. *Physical review B*, *54*(16), 11169.

84. Kresse, G., & Joubert, D. (1999). From ultrasoft pseudopotentials to the projector augmented-wave method. *Physical Review B*, *59*(3), 1758.

85. Perdew, J. P., Burke, K., & Ernzerhof, M. (1996). Generalized gradient approximation made simple. *Physical review letters*, *77*(18), 3865.

86. Alfè, D. (2009). PHON: A program to calculate phonons using the small displacement method. *Computer Physics Communications*, *180*(12), 2622-2633.

87. Qiao, X. F., Li, X. L., Zhang, X., Shi, W., Wu, J. B., Chen, T., & Tan, P. H. (2015). Substrate-free layer-number identification of two-dimensional materials: A case of Mo0. 5W0. 5S2 alloy. *Applied Physics Letters*, *106*(22), 223102.

88. Feng, Q., Zhu, Y., Hong, J., Zhang, M., Duan, W., Mao, N., ... & Jin, C. (2014). Growth of Large-Area 2D MoS2 (1-x) Se2x Semiconductor Alloys. *Advanced Materials*, *26*(17), 2648-2653.

89. Zhu, W., Perebeinos, V., Freitag, M., & Avouris, P. (2009). Carrier scattering, mobilities, and electrostatic potential in monolayer, bilayer, and trilayer graphene. *Physical Review B*, *80*(23), 235402.

90. Misse, P., Berthebaud, D., Lebedev, O. I., Maignan, A., & Guilmeau, E. (2015). Synthesis and Thermoelectric Properties in the 2D Ti1−xNbxS3 Trichalcogenides. *Materials*, *8*(5), 2514-2522.

91. Lipatov, A., Wilson, P. M., Shekhirev, M., Teeter, J. D., Netusil, R., & Sinitskii, A. (2015). Few-layered titanium trisulfide (TiS 3) field-effect transistors. *Nanoscale*, *7*(29), 12291-12296.